Journal of Medicinal Chemistry

Article

Cite This: J. Med. Chem. XXXX, XXX, XXX−XXX

pubs.acs.org/jmc

Discovery of Conformational Control Inhibitors Switching off the Activated c-KIT and Targeting a Broad Range of Clinically Relevant c-KIT Mutants

Tsung-Sheng Wu,[†] Wen-Hsing Lin,[†] Hui-Jen Tsai,[‡,§] Ching-Cheng Hsueh,[†] Tsu Hsu,[†] Pei-Chen Wang,[†] Hui-You Lin,[‡] Yi-Hui Peng,[†] Cheng-Tai Lu,[†] Lung-Chun Lee,[†] Chih-Hsiang Tu,[†] Fang-Chun Kung,[†] Hui-Yi Shiao,[†] Teng-Kuang Yeh,[†] Jen-Shin Song,[†] Jia-Yu Chang,[†] Yu-Chieh Su,[†] Li-Tzong Chen,[‡,∥] Chiung-Tong Chen,[†] Weir-Torn Jiaang,*[,†] and Su-Ying Wu*[,†]

[†]Institute of Biotechnology and Pharmaceutical Research, National Health Research Institutes, 35, Keyan Road, Zhunan Town, Miaoli County 350, Taiwan R.O.C.

[‡]National Institute of Cancer Research, National Health Research Institutes, Tainan City 704, Taiwan R.O.C.

[§]Division of Hematology/Oncology, Department of Internal Medicine, National Cheng Kung University Hospital, Tainan City 704, Taiwan R.O.C

[∥]Institute of Molecular Medicine, National Cheng Kung University, Tainan City 704, Taiwan R.O.C.

Supporting Information

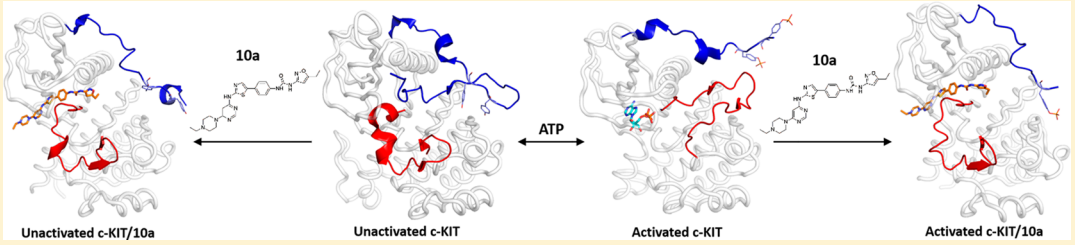

ABSTRACT: Drug resistance due to acquired mutations that constitutively activate c-KIT is a significant challenge in the treatment of patients with gastrointestinal stromal tumors (GISTs). Herein, we identified 1-(5-ethyl-isoxazol-3-yl)-3-(4-{2-[6-(4-ethylpiperazin-1-yl)pyrimidin-4-ylamino]-thiazol-5-yl}phenyl)urea (**10a**) as a potent inhibitor against unactivated and activated c-KIT. The binding of **10a** induced rearrangements of the DFG motif, αC-helix, juxtamembrane domain, and the activation loop to switch the activated c-KIT back to its structurally inactive state. To the best of our knowledge, it is the first structural evidence demonstrating how a compound can inhibit the activated c-KIT by switching back to its inactive state through a sequence of conformational changes. Moreover, **10a** can effectively inhibit various c-KIT mutants and the proliferation of several GIST cell lines. The distinct binding features and superior inhibitory potency of **10a**, together with its excellent efficacy in the xenograft model, establish **10a** as worthy of further clinical evaluation in the advanced GISTs.

INTRODUCTION

Receptor tyrosine kinases (RTKs) are cell membrane receptors conducting signaling of growth factors, cytokines, and hormones to orchestrate normal cell development and behavior in a highly regulated manner.[1] Perturbation of RTKs-mediated signaling is characteristic in many disorders, including a significant proportion of human cancers.[2] On the basis of sequence similarity and structural homology, the proto-oncogenic protein c-KIT is categorized as a type III RTK comprised of five IgG-like extracellular domains, a transmembrane helix followed by an autoinhibitory juxtamembrane (JM) domain, and a cytoplasmic kinase domain.[3]

The catalytic activity of c-KIT remains autoinhibited[4] until its cognate ligand, stem cell factor (SCF), binds to and initiates a series of activation processes. Binding of SCF initiates homodimerization of c-KIT in a divalent manner, bringing each of the c-KIT monomers in close proximity and rearranging them in a proper orientation critical for the following intracellular activation events.[5] While how the extracellular conformational changes transmit and initiate intracellular activation of c-KIT remains unresolved, it is clear that upon SCF stimulation, the JM domain is relieved from an autoinhibited position that impedes the activation loop (A-loop) for adopting the activated conformation.[6] The A-loop in turn switches from an inactive position that sterically hinders the ATP-binding cleft to a proper activated position to allow a γ-phosphate of ATP to be transferred to tyrosine residues of protein substrates.[4,7] While these two major conformational changes initiate the catalytic activity of the c-

Received: November 26, 2018

Table 1. Inhibition of c-KIT Enzymatic Activity and GIST-T1 Cell Proliferation by 10a and the Analogues

	compound	IC_{50} (nM)[a]	GI_{50} (nM)[a]
		c-KIT	GIST-T1[b]
10a	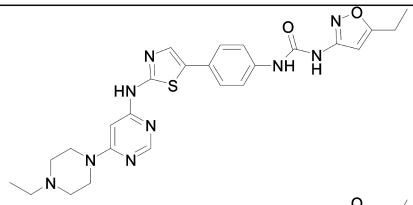	82	2.2
10b	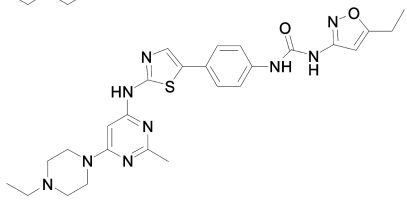	97	3.2
10c	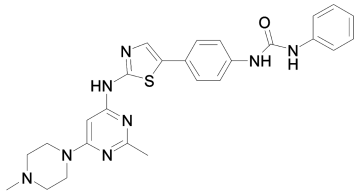	20	5.4
10d	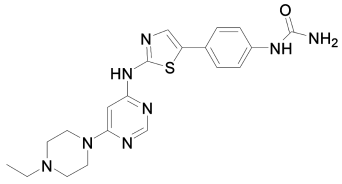	98	86
10e	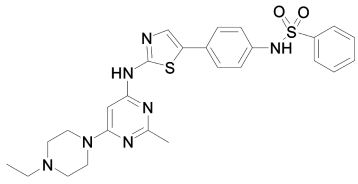	54	42
10f	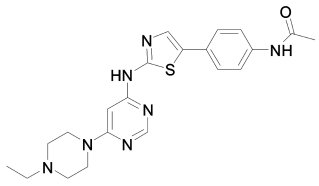	130	25
10g	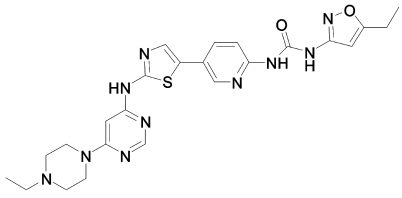	43	1.0
18	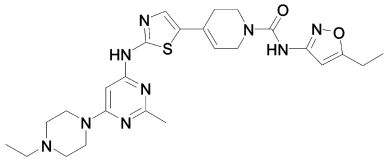	82	4.9

DOI: 10.1021/acs.jmedchem.8b01845
J. Med. Chem. XXXX, XXX, XXX−XXX

Table 1. continued

compound		IC_{50} (nM)[a] c-KIT	GI_{50} (nM)[a] GIST-T1[b]
22	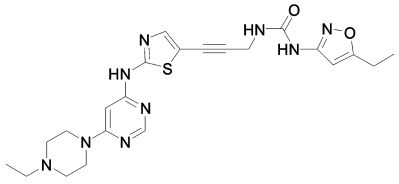	38	9.9
24	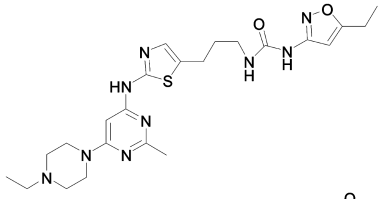	50	10
10h	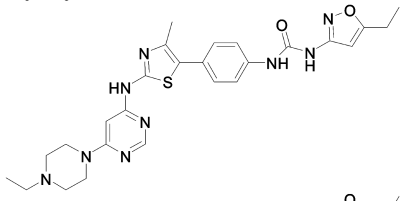	122	3.3
11	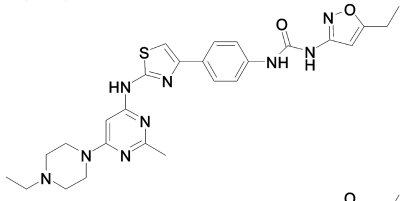	950	>1,000
10i	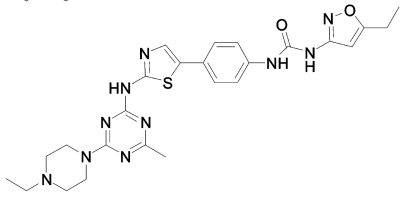	86	13
10j	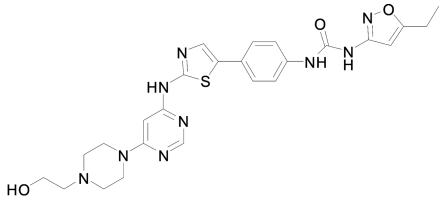	71	3.3
10k	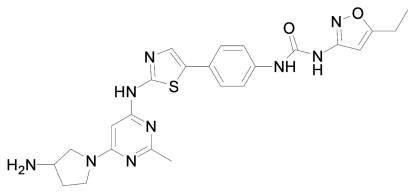	15	6.4
Sunitinib	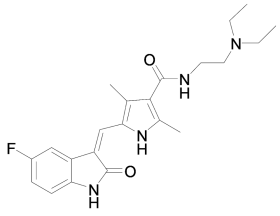	48	38

[a]Values of IC_{50} and GI_{50} are expressed as the mean of three independent experiments and are within ±15%. [b]GIST cell line: heterozygous deletion of V560-Y578.

DOI: 10.1021/acs.jmedchem.8b01845
J. Med. Chem. XXXX, XXX, XXX−XXX

Scheme 1[a]

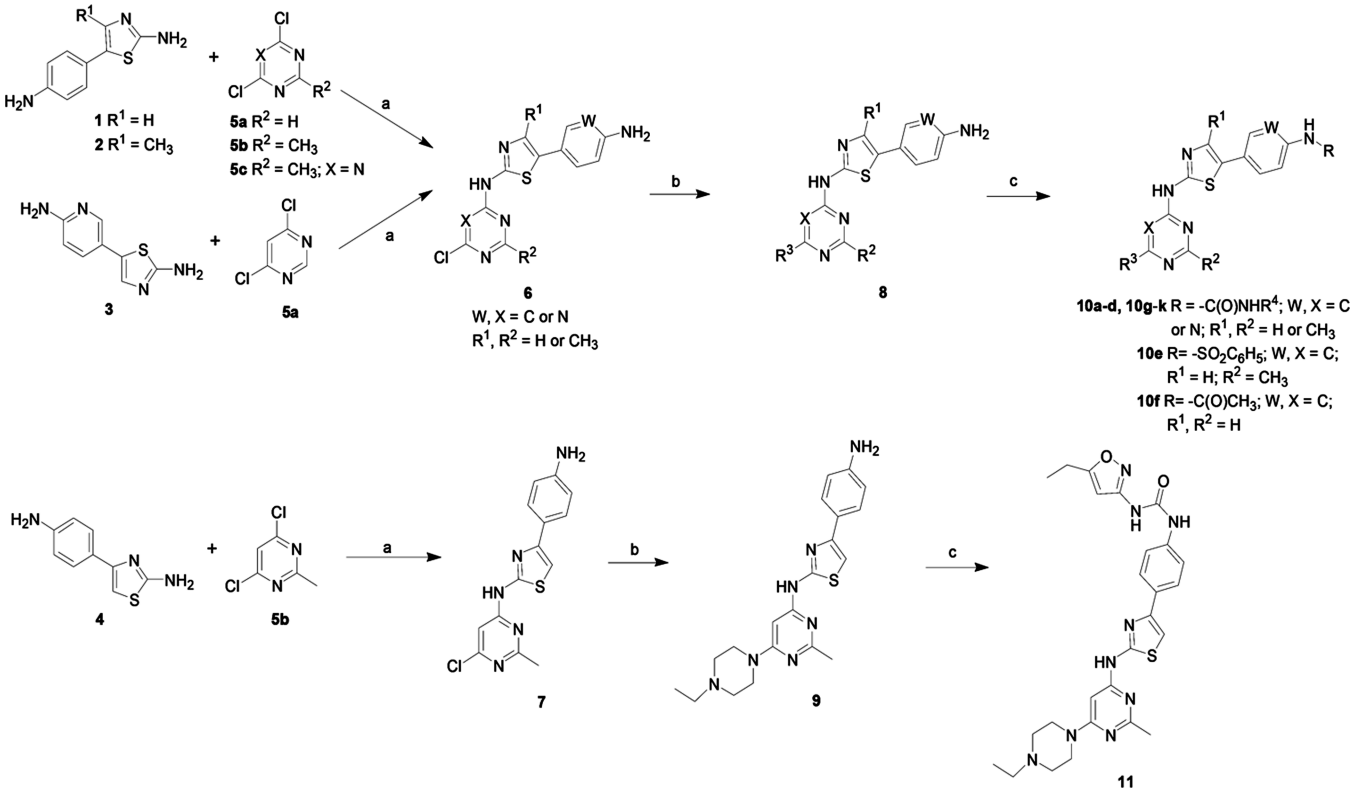

[a]Reagents and conditions: (a) NaH, THF, 0 °C; (b) 2° amines, pyridine, 80 °C; (c) pyridine, (5-ethylisoxazol-3-yl)carbamic acid 4-nitro-phenyl ester for **10a**,**b**, **10g**−**k**, and **11**, phenyl isocyanate for **10c**, benzenesulfonyl chloride for **10e**, acetyl chloride for **10f**, rt. KOCN, AcOH, H_2O for **10d**.

KIT, a series of autophosphorylation of tyrosine residues at JM domain and A-loop are considered as the necessity for full activation and as a stabilizer for the active conformation of c-KIT.[8]

Aberrant activation of c-KIT activity due to naturally occurring or drug-induced mutations plays an important role in etiology and drug resistance in gastrointestinal stromal tumors (GISTs).[9] The most common primary mutations in GISTs occur in the exon 11 of *c-KIT*.[10] Given that exon 11 encodes the JM domain of c-KIT, these mutations may alter the autoinhibitory properties of the JM domain and/or compromise the binding of negative regulators that dephosphorylate and inactivate the c-KIT kinase activity,[11] either of which contributes to the transformation of c-KIT to its active form.[10] Mutations in *cKIT* exon 9, which encodes the IgG-like extracellular domain D5, account for the second most common primary *c-KIT* mutations in GISTs.[12,13] These mutations may enhance the interaction between D5 domains and promote c-KIT dimerization and activation.[5]

Imatinib was approved and implemented as the first line treatment[14] for patients with resectable primary GISTs[15] as well as those with unresectable or advanced metastatic GISTs[16] caused by mutations at exon 11 of *c-KIT*.[17] This first line treatment, however, induces mutations in *c-KIT* gene that decrease c-KIT sensitivity to imatinib.[18,19] In contrast to the primary *c-KIT* mutations, these acquired secondary mutations are mostly found in exon 13/14 and exon 17 of *c-KIT*, which encode the kinase catalytic pocket and A-loop, respectively, and are responsible for the failure in the treatment of GISTs by different mechanisms.[20] For example, substitution of Val654 in the ATP binding pocket to alanine may result in loss of c-KIT-drug interaction,[21] whereas substitutions of gatekeeper Thr670 to residues with a bulkier side chain, such as isoleucine, may induce steric clashes,[22] and its hydrophobicity may stabilize c-KIT in an activated conformation.[23] In contrast, mutations in the A-loop, such as D816H, shift the c-KIT activation equilibrium from inactive to the active state, rendering it insensitive to many inhibitors.[24,25] Although the second line sunitinib[26] and the third line regorafinib[27] have been approved and implemented for treatment of the refractory GISTs, sunitinib was shown to be ineffective against c-KIT A-loop mutants,[24] and regorafinib treatment was found to be only modestly beneficial.[27] Accordingly, there is an urgent need for novel c-KIT inhibitors that effectively target a broad spectrum of c-KIT mutants and improve the survival of patients with advanced GISTs.[28]

The concept of designing conformational control inhibitors to target the activated form of kinases and enable the inhibition of a wide range of kinase mutants has been proposed. Indeed, a class of inhibitors targeting the "switch control pocket"[29] to force the activated p38-MAP kinase into a conformation that resembled its type II inactive state was discovered.[30,31] In the case of BCR-ABL tyrosine kinase, a switch control inhibitor showed potency against several clinically relevant chronic myeloid leukemia (CML) related mutants.[32] In the case of c-KIT, although several inhibitors with different chemical scaffolds have been discovered,[28] a mechanistic understanding of how the activated c-KIT and various c-KIT mutants can be inhibited is still unclear. Therefore, discovery of novel

DOI: 10.1021/acs.jmedchem.8b01845
J. Med. Chem. XXXX, XXX, XXX−XXX

Scheme 2[a]

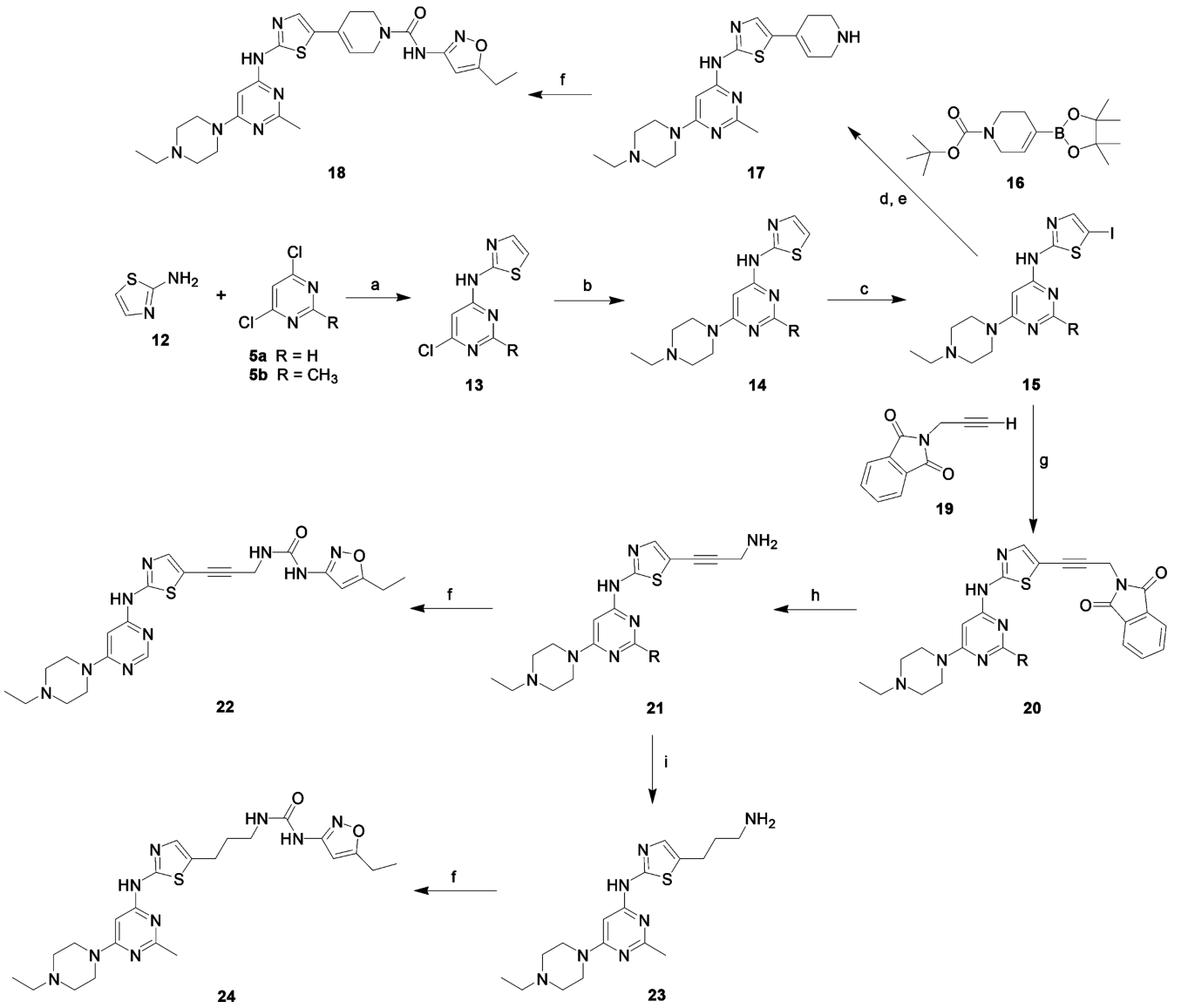

[a]Reagents and conditions: (a) NaH, THF, rt; (b) 1-ethylpiperazine, pyridine, 65 °C; (c) NIS, $CHCl_3$, rt; (d) $Pd(dppf)Cl_2$, Na_2CO_3, 1,4-dioxane, 80 °C; (e) TFA, CH_2Cl_2, rt; (f) pyridine, (5-ethylisoxazol-3-yl)carbamic acid 4-nitro-phenyl ester, rt; (g) $Pd(PPh_3)_4$, CuI, NEt_3, THF, rt; (h) H_2N-NH_2, THF, rt; (i) H_2, $Pd/BaSO_4$, MeOH, rt.

conformational control inhibitors against c-KIT with support of structural evidence is needed.

In this study, we synthesized a series of 5-phenyl-thiazol-2-ylamine based compounds bearing a urea substituent, and identified **10a** as a potent c-KIT inhibitor on the basis of its enzymatic and cellular activities. The crystal structure of c-KIT in complex with **10a** revealed **10a** as a type II inhibitor, in which **10a** binds to c-KIT in a "DFG-out" inactive conformation. More importantly, binding of **10a** shuts off the activities of the activated c-KIT by inducing dramatic conformational changes that switch the activated c-KIT back to its inactive state. Moreover, **10a** was found to effectively inhibit activities of a broad spectrum of c-KIT mutants, including those bearing mutations in the A-loop, as well as the proliferation of several GIST cell lines and the growth of tumors in a xenograft mouse model. These results provided novel structural insights into the compound-induced inactivation of the activated c-KIT and revealed the therapeutic potential of **10a** in treatment of advanced GISTs.

RESULTS

Identification of 10a and Its Analogues as c-KIT Inhibitors. A class of 5-phenyl-thiazol-2-ylamine pyrimidine derivatives[33] has been utilized as a versatile template for the development of kinase inhibitors. On the basis of this scaffold, urea-substituted series of compounds were synthesized and they were identified as c-KIT inhibitors by our in-house kinase screening programs. Among these derivatives, **10a** exhibited high potency against c-KIT enzymatic (IC_{50} = 82 nM) and cellular (GI_{50} = 2.2 nM) activities (Table 1).

The general synthetic route for **10a** and its analogues is shown in Scheme 1 and 2. Compounds **10a**–**k** and **11** were synthesized based on our previous publication with modification.[33] The synthesis began with the preparation of 4- or 5-

DOI: 10.1021/acs.jmedchem.8b01845
J. Med. Chem. XXXX, XXX, XXX−XXX

aromatic ring substituted thiazol-2-ylamines **1**−**2**,[34] **3**,[35] or **4**[36] according to previously published protocols. 4,6-Disubstituted pyrimidine **8** was coupled with (5-ethylisoxazol-3-yl)carbamic acid 4-nitrophenyl ester in pyridine to afford ureas **10a**−**c** and **10g**−**k**. The treatment of 4,6-disubstituted pyrimidine **8** with potassium cyanate in acetic acid/water, benzenesulfonyl chloride in pyridine, and acetyl chloride in pyridine afforded the final urea **10d**, sulfonamide **10e**,[33] and amide **10f**, respectively. The synthetic route to 5-substituted thiazol-2-ylamine pyrimidines **18**, **22**, and **24** (Table 1) is shown in Scheme 2. Treatment of thiazol-2-ylamine **12** with 4,6-dichloropyrimidines **5** in the presence of NaH and THF at room temperature afforded 4-monosubstituted pyrimidine derivatives **13**. The treatment of derivatives **13** with 1-ethylpiperazine in pyridine at 80 °C yielded 4,6-disubstituted pyrimidines **14**. Electrophilic iodination of thiazole using *N*-iodosuccinimide (NIS) in $CHCl_3$ afforded 5-iodothiazol-2-ylamine **15**, which was coupled with *N*-Boc protected 1,2,3,6-tetrahydropyridyl borane **16** or phthalimide-protected prop-2-ynylamine **19** to yield *N*-Boc protected 5-(1,2,3,6-tetrahydropyridin-4-yl)thiazol-2-ylamine pyrimidine **17** or phthalimide-protected 5-(3-aminoprop-1-ynyl)thiazol-2-ylamine pyrimidine **20**, respectively. Deprotection of Boc-**17** or phthalimide-protected **20** using TFA or hydrazine followed by coupling with (5-ethylisoxazol-3-yl)carbamic acid 4-nitrophenyl ester afforded the final pyrimidine urea **18** or **22**, respectively. Unsaturated prop-2-ynylamine **21** reacted with hydrogen in the presence of Pd catalyst in MeOH to provide butylamine **23**, which was coupled with (5-ethylisoxazol-3-yl)carbamic acid 4-nitro-phenyl ester to give final pyrimidine urea **24**.

Compound **10a** and the analogues were evaluated in kinase activity and cell proliferation assays to facilitate the elucidation of structure−activity relationships. As shown in Table 1, 2-methylpyrimidine **10b**[33] exhibited similar inhibitory activities against wild type c-KIT kinase and GIST-T1 cells as **10a**. Phenyl-substituted urea **10c**[33] showed potent inhibition against c-KIT. Removing the 5-ethylisoxazole moiety of **10a** (**10d**), replacing the urea moiety of **10a** with sulfonamide (**10e**)[33] or amide moiety (**10f**) did not significantly affect the inhibition of c-KIT kinase activity but did result in reduced cellular potency. With maintenance of the urea moiety, replacement of **10a**'s phenyl ring by a pyridin-2-yl ring (**10g**), a 1,2,3,6-tetrahydropyridine ring (**18**), or linear alkyl groups, such as propynyl (**22**) and propyl (**24**), did not significantly affect the inhibitory potency against c-KIT kinase and GIST-T1 cells.

Next, we examined effects of substitutions on the thiazole ring and compared the potencies of compounds **10h** and **11** with **10a**. Compound **10h**, with a methyl substituent at the fourth position of the thiazole ring, exhibited a slightly reduced and comparable potency against c-KIT kinase and GIST-T1 cells, respectively. By contrast, a significant decrease in both enzymatic and cellular potency was observed when the phenylurea tail of **10a** was moved from the fifth position to the fourth position (**11**) of the thiazole ring. The importance of the pyrimidine moiety of **10a** was revealed by the observation that changing of pyrimidine moiety of **10a** to 2-methyl-1,3,5-triazine (**10i**) led to 6-fold decrease of potency against GIST-T1 cells. Finally, the effects of water-solubilizing groups were investigated. *N*-(2-Hydroxyethyl)piperazine **10j** exhibited a potency that was similar to **10a** in the enzymatic and cellular assays. Compound **10k**[33] bearing a primary pyrrolidin-3-ylamine group increased the enzymatic inhibition against c-KIT but slightly decreased the cellular activity as compared to **10a**.

Among the analogues listed in Table 1, only **10g** showed show slightly better activities than **10a** both in enzymatic and cellular assays. However, **10g** has low synthetic yield as compared to **10a**. Moreover, **10c** and **10k** have poor PK profiles[33] although they exhibited potent inhibition against c-KIT. Therefore, compound **10a** was selected for further biological activity and in vivo efficacy studies.

Crystal Structure of c-KIT Kinase in Complex with 10a. The excellent enzymatic and cellular potency of **10a** against c-KIT and GIST-T1 cells prompted us to further investigate the molecular mechanisms underlying this activity. After expression and purification, the recombinant c-KIT proteins were found to be unphosphorylated and in their unactivated form (Supporting Information, Figure S1, lane 1). The crystal structure of the unactivated c-KIT kinase domain in complex with **10a** (hereafter referred to as unactivated c-KIT/**10a**) was determined in a resolution of 2.10 Å. Data collection and refinement statistics are summarized in Table 2.

Table 2. Statistics of X-ray Diffraction Data and Structure Refinement for c-KIT Complex Structure

	unactivated c-KIT/**10a** (6ITT)	activated c-KIT/**10a** (6ITV)
resolution (Å)	28.43−2.10	26.77−1.88
space group	$P2_12_12_1$	$P4_32_12$
unit cell		
a, *b*, *c* (Å)	62.63, 63.09, 196.81	59.86, 59.86, 197.98
α, *β*, *γ* (deg)	90, 90, 90	90, 90, 90
unique reflections	45999 (4548)	30279 (2935)
I/σ	21.77 (2.48)	25.14 (2.45)
R_{merge} (%)	5.7 (59.6)	5.5 (65.4)
completeness (%)	99.5 (100.0)	99.7 (100.0)
Wilson *B*-factor	36.66	30.42
R_{work}/R_{free}	0.1862/0.2346	0.1798/0.2306
rmsd (bond) (Å)	0.008	0.006
rmsd (angle) (deg)	0.976	0.828
Ramachandran favored (%)	97.63	98.29
MolProbility clash score	6.05	2.08
MolProbility overall score	1.41	0.98

The overall structure shows that **10a** binds to the unactivated c-KIT at the ATP-binding pocket located between the N- and C-lobe (Figure 1B). In addition, **10a** stabilizes c-KIT in an inactive conformation, wherein the A-loop is retained in a DFG-out inactive conformation (Figure 1B, magenta), resembling the autoinhibited conformation of the native form of unactivated c-KIT[4] (Figure 1A, magenta, hereafter referred to as unactivated c-KIT; PDB 1T45). Instead of an ordered and compact hairpin loop conformation observed in the unactivated c-KIT (Figure 1A, blue), the N-terminal segment (Tyr547-Glu562) of the JM domain of unactivated c-KIT/**10a** is exposed to the solvent region and is too flexible to be detected in the crystal structure (Figure 1B, blue).

The pharmacophore of **10a** can be divided into a solvent-exposed headgroup (ethylpiperazine), a hinge scaffold (thiazolylamine), a middle linker (phenyl), and a hydrogen-bonding moiety (urea) along with a tail group (5-ethyl-

DOI: 10.1021/acs.jmedchem.8b01845
J. Med. Chem. XXXX, XXX, XXX−XXX

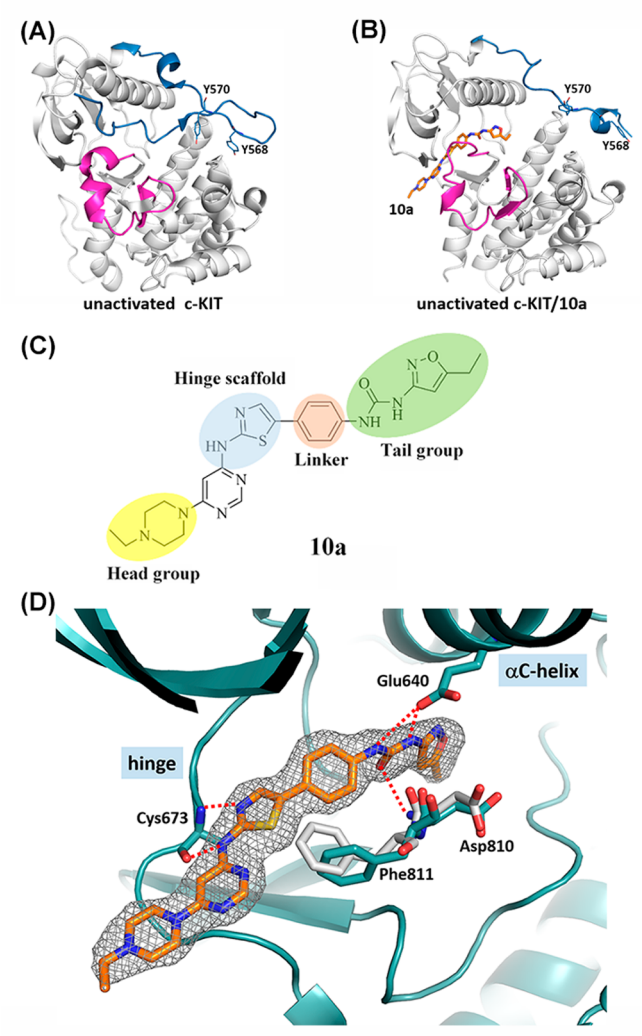

Figure 1. Overall structure of the (A) apo form (PDB 1T45) and (B) **10a**-bound unactivated c-KIT (PDB 6ITT). The JM domain and A-loop are shown in blue and magenta, respectively. (C) Pharmacophore of **10a**: solvent-exposed headgroup (yellow), hinge scaffold (light blue), linker (light salmon), and tail group (light green). (D) The structure of the unactivated c-KIT kinase domain in complex with **10a**. Compound **10a** is shown in orange, with its electron density map (1.0 sigma). The H-bonds between c-KIT and **10a** are shown in red dash lines. Residue Asp810 and Phe811 of the apo form of unactivated c-KIT are shown in gray.

isoxazole) (Figure 1C). The binding features of **10a** to the unactivated c-KIT are shown in Figure 1D. The thiazolylamine scaffold of **10a** forms two H-bonds with the backbone of Cys673 in the hinge region of c-KIT. In addition, the tail group of **10a** occupies the back pocket of the ATP-binding site by forming three more H-bonds between the nitrogen and oxygen of the urea group and the side chain of Glu640 and the backbone of Asp810, respectively. Upon binding of **10a**, the rearranged Phe811 forms a perpendicular "edge-to-face" aromatic interaction with the phenyl ring of **10a** (Figure 1D). The ethylpiperazine group of **10a** is exposed in the solvent region in the crystal structure, which is usually utilized to improve the physiochemical properties of compounds.[37] The above features, especially the interaction network of **10a** and Glu640 at the αC-helix and Asp810 of the DFG motif, have characterized **10a** as a type II kinase inhibitor.[38]

Our previous SAR analysis revealed that the inhibitory potency significantly decreased when the phenylurea group of **10a** was switched from the fifth to the fourth position on the thiazole ring (**11**) (Table 1). According to our crystal structure, the distance between the fourth carbon of the thiazole ring of **10a** with the surrounding residues ranges from 3.3 to 4.7 Å (Supporting Information, Figure S2A). To maintain the critical H-bond between the nitrogen on the thiazole ring and Cys673 in the hinge region, the thiazole ring must remain in the original position with its nitrogen facing to the backbone of Cys673. Accordingly, if this conserved H-bond has to be maintained between the nitrogen atom of thiazole ring in **11** and Cys673, the linker and tail groups on the fourth position of the thiazole ring of **11** would cause serious clashes with the surrounding residues (Supporting Information, Figure S2B). To avoid this, the thiazole ring of **11** would need to flip into a new orientation that allows the following linker and tail groups to properly fit into the binding site, but this results in a loss of the critical H-bond with Cys673 (Supporting Information, Figure S2C). Either of the above scenarios are expected to diminish binding affinity of **11** to c-KIT, which rationalizes the 10 times lower inhibitory potency of **11** to c-KIT compared to **10a** (Table 1).

On the basis of the observation of short distances between the fourth carbon of the thiazole ring of **10a** with the surrounding residues (Supporting Information, Figure S2A), addition of a methyl group on the fourth position of the thiazole ring (**10h**) is also expected to cause steric effects with the surrounding residues, such as Glu671. To avoid the steric effects, **10h** would adopt a different conformation, as supported by our molecular docking analysis (Figure S3). Although **10h** was docked into c-KIT in a highly similar orientation as **10a**, the thiazole ring moved away from the hinge region to accommodate the additional methyl group of **10h** (Supporting Information, Figure S3A, red arrow), resulting in a weaker H-bond between thiazolylamine N3 and Cys673/N. Moreover, the additional methyl group of **10h** induced a rotation of the phenyl linker, consequently directing the tail group away from the αC-helix and leading to loss of one of the H-bonds with Glu640 (compare Supporting Information, Figure S3C with S3B). The steric hindrance induced by the additional methyl group of **10h**, together with its possible adjustments indicated by molecular docking analysis, are plausible explanations for the reduced inhibitory potency of **10h** to c-KIT when compared to **10a** (Table 1).

Substitution of the phenyl linker of **10a** with six-membered carbon ring (**10g** and **18**) or three-carbon alkyl group (**22** and **24**) did not reduce the inhibitory potency (Table 1), indicating that replacement of the linker with a moiety of optimum length size to properly position the hinge scaffold and the urea group for hydrogen bond formation to be practical. Indeed, cocrystallized structures revealed that many type II inhibitors bear linker moieties comprising an aliphatic chain or aromatic ring with 3−5 chemical bonds in length.[38]

The crystal structure and the SAR study consistently revealed the importance of the tail group in the activity of **10a** (Figure 1D and Table 1). Removal of the ethylisoxazole group of **10a** to give **10d** had little effect on the inhibitory activity against c-KIT, indicating the intact urea group but not the ethylisoxazole group to be important for maintaining the H-bond network and contributing to the potency. In contrast, substitution of the urea group of **10d** with an amide group to give **10f** reduced the inhibitory potency against c-KIT activity,

DOI: 10.1021/acs.jmedchem.8b01845
J. Med. Chem. XXXX, XXX, XXX−XXX

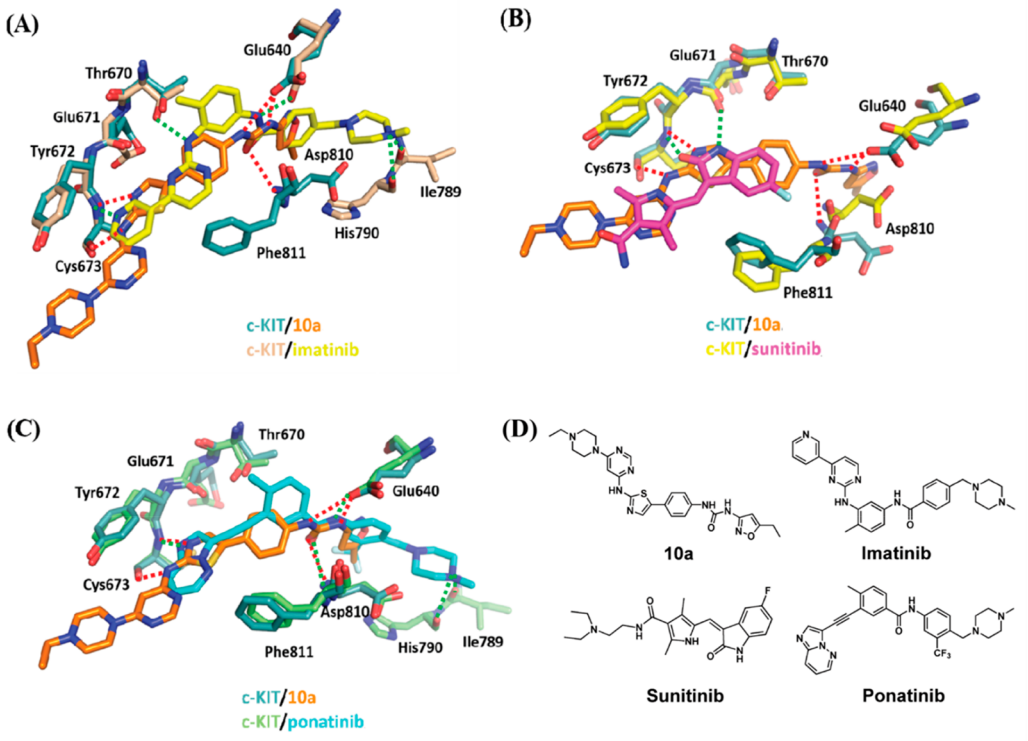

Figure 2. (A) Comparison of the structure of c-KIT/**10a** and c-KIT/imatinib. (B) Comparison of the structure of c-KIT/**10a** and c-KIT/sunitinib. (C) Comparison of the structure of c-KIT/**10a** and c-KIT/ponatinib. (D) Chemical structures of **10a**, imatinib, sunitinib. and ponatinib. Hydrogen bonds between c-KIT and **10a** are shown with red dashed lines. Hydrogen bonds between c-KIT and imatinib (or sunitinib or ponatinib) are shown with green dashed lines.

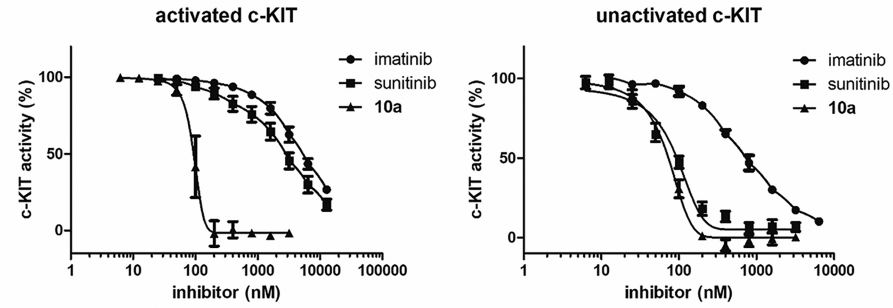

	Imatinib	Sunitinib	**10a**
unactivated c-KIT	769 ± 86	80 ± 6.8	69 ± 8.7
activated c-KIT	5210 ± 619	3021 ± 669	92 ± 11

Figure 3. Determination of IC_{50} of inhibitors to the unactivated and activated c-KIT. IC_{50} of inhibitors to c-KIT were determined as the concentrations (nM) of inhibitors required to inhibit 50% of c-KIT kinase activity. Values are expressed as means ± SEM of three independent assays.

suggesting that the intact urea group may provide optimal interactions of **10a** to c-KIT.

Comparison with the Structures of Other Inhibitors Bound to c-KIT. First, the structure of c-KIT/**10a** was compared with the structures of c-KIT/imatinib (PDB 1T46). Superimposing of these two structures revealed that the pyridine and pyrimidin-2-ylamine groups of imatinib occupied a similar position as that of the thiazolylamine and phenyl groups of **10a** and interacted with the hinge region of c-KIT (Figure 2A). The amide group of imatinib formed one hydrogen bond with Glu640, while the interaction network of **10a** with Glu640 and Asp810 was more extensive with three hydrogen bonds. Moreover, unlike **10a**, instead of exposing the headgroup to the solvent region, imatinib extended deeply into the binding pocket and formed interactions with Ile789 and His790. The structure of c-KIT/**10a** was also compared with that of c-KIT/sunitinib (PDB 3G0E). The pyrrole and indole groups of sunitinib overlapped with the pyrimidine and thiazolylamine groups of **10a**, respectively (Figure 2B). The (2-diethylaminoethyl)amine group of sunitinib was exposed to

DOI: 10.1021/acs.jmedchem.8b01845
J. Med. Chem. XXXX, XXX, XXX−XXX

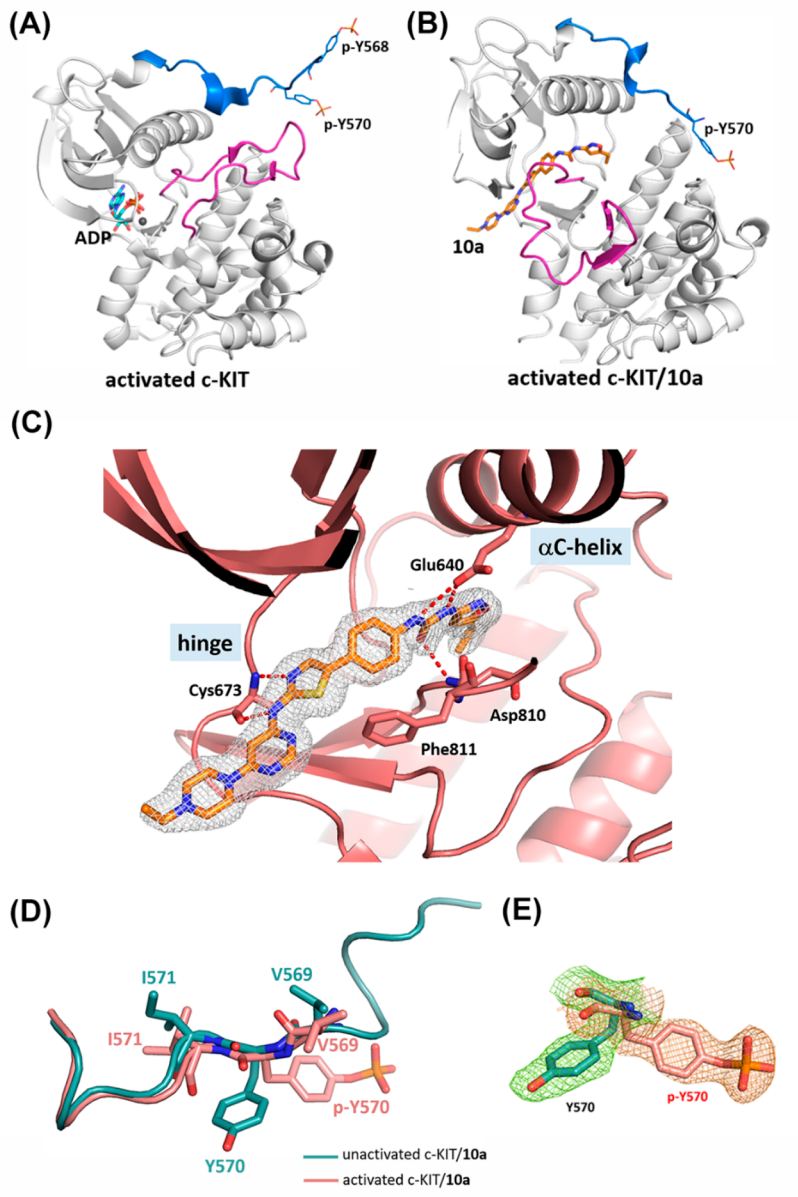

Figure 4. Overall structure of the (A) native form (PDB 1PKG) and (B) **10a**-bound (PDB 6ITV) activated c-KIT. The JM domain and A-loop are shown in blue and magenta, respectively. (C) The structure of the activated c-KIT in complex with **10a**. Compound **10a** is shown in orange with its electron density map (1.0σ). The H-bonds between c-KIT and **10a** are shown in red dash lines. (D) Structural comparison of the N-terminal JM domain of the unactivated c-KIT/**10a** (light teal) and activated c-KIT/**10a** (pink). (E) Structural differences with electron density maps (0.9σ) of the Tyr570 and phospho-Tyr570 in the unactivated and activated c-KIT.

the solvent region and was not observable in the crystal structure. Sunitinib interacted with the hinge region and the DFG-motif of c-KIT and kept c-KIT in a DFG-out conformation. However, the interactions of sunitinib with Glu640 were absent. Moreover, the structure of c-KIT/**10a** was compared with that of c-KIT/ponatinib (PDB 4U0I). The imidazo[1,2-*b*]pyridazine group of ponatinib occupied a similar position as that of the thiazolylamine groups of **10a** and interacted with the hinge region of c-KIT (Figure 2C). The amide group of ponatinib also formed interactions with Glu640. The piperazine group of ponatinib extended deeply into the binding pocket while the ethylpiperazine group of **10a** exposed toward the solvent region.

Compound 10a Potently Inhibits the Activated c-KIT. Studies have revealed that inhibitors with high activities against the activated form of kinases often also show high potency against many drug-induced kinase mutants.[32] This prompted us to further investigate whether compound **10a** could inhibit the activated c-KIT with a similar potency as to the unactivated c-KIT. To obtain the activated c-KIT, the purified unactivated c-KIT recombinant proteins were incubated with an excess amount of ATP, and their phosphorylation was confirmed by Western blot analysis (Supporting Information, Figure S1). In addition to phosphorylation, the activation of c-KIT was further confirmed by the observation that imatinib and sunitinib inhibited the activated c-KIT with a significantly lower potency compared to that of the unactivated c-KIT (Figure 3), which is consistent with the previous reports.[24] In contrast to imatinib and sunitinib, compound **10a** was found to inhibit the enzymatic activities of both unactivated and

DOI: 10.1021/acs.jmedchem.8b01845
J. Med. Chem. XXXX, XXX, XXX−XXX

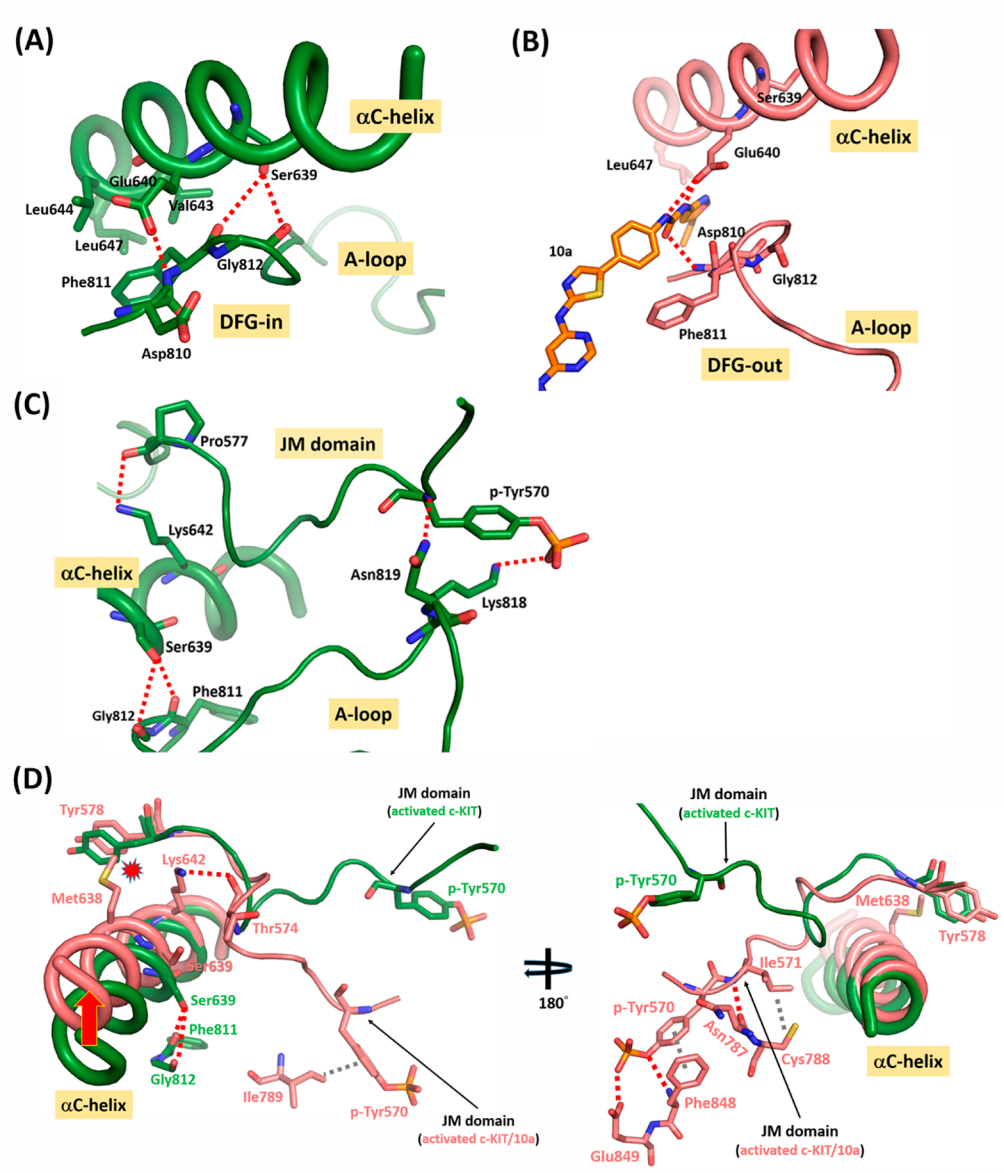

Figure 5. Binding of **10a** to the activated c-KIT induced a sequence of conformational changes in the DFG motif, αC-helix and JM domain. (A) Interactions of A-loop with αC-helix stabilized A-loop in a DFG-in conformation in the activated c-KIT structure (PDB 1PKG). (B) Interaction network between αC-helix, **10a**, and DFG motif upon binding of **10a** to the activated c-KIT (PDB 6ITV). (C) In addition to the interactions with αC-helix, Lys818, and Asn819 of the activated A-loop were stabilized by forming strong interactions with p-Tyr570 of the activated JM domain. (D) Binding of **10a** moved αC-helix (red arrow), which caused a steric effect toward JM domain (red explosion drawing). The JM domain was then rearranged and stabilized in a new position (pink) by forming H-bond (red dash line) and hydrophobic (gray dash line) interactions with residues at the C-lobe.

activated c-KIT with similarly high potencies (Figure 3). The ability of **10a** to potently inhibit the activated c-KIT suggested a possibility that **10a** would also inhibit the constitutively active c-KIT mutants.

Compound 10a Induces the Conformational Changes That Switch the Activated c-KIT to Its Inactive State. On the basis of the enzymatic results that **10a** potently inhibits the activated c-KIT, we next investigated the structural mechanisms underlying this important observation. The activated c-KIT proteins were cocrystallized with **10a** and a high-quality crystal structure (hereafter referred to as activated c-KIT/**10a**) with a resolution of 1.88 Å was obtained (Table 2). Surprisingly, the activated c-KIT/**10a** (Figure 4B) was found to no longer adopt the activated conformation[7] (Figure 4A; PDB 1PKG). Instead, the overall structure closely resembles that of the unactivated c-KIT/**10a** (Figure 1B). Moreover, the binding mode of **10a** to the activated c-KIT was almost identical to that observed in the unactivated c-KIT/**10a** structure (Figure 1D), wherein the interactions between the thiazolylamine scaffold of **10a** and the Cys673 of the hinge region, as well as those of the conventional Glu640−**10a**−Asp810 interaction network, were properly formed (Figure 4C). However, the most significant difference between the activated c-KIT/**10a** and unactivated c-KIT/**10a** structures was found in the JM domain (Figure 4D), wherein the Ile571, p-Tyr570, and Val569 residues were orientated differently and the N-terminal segment (Tyr547-Asn566) was absent in the activated c-KIT/**10a** crystal structure. In addition, the electron

DOI: 10.1021/acs.jmedchem.8b01845
J. Med. Chem. XXXX, XXX, XXX−XXX

density map of the phosphate group of the p-Tyr570 can be clearly seen (Figure 4E, pink), which provided direct evidence that the proper phosphorylation and activation of the c-KIT proteins had taken place.

To elucidate the mechanism underlying the **10a**-induced on-to-off switch of the activated c-KIT, the structure of activated c-KIT/**10a** was compared with the native form of the activated c-KIT[7] (PDB 1PKG) in detail. In the native form of the activated c-KIT, the hydrolyzed ADP after *trans*-autophosphorylation is retained in the ATP binding pocket (Figure 4A). The JM domain is phosphorylated and a large part of it is exposed to the solvent region (Figure 4A, blue). With a DFG-in conformation,[7] the activated A-loop (Figure 4A, magenta) extends into a space that was occupied by the autoinhibited JM domain of the unactivated c-KIT (Figure 1A, blue) and is stabilized by αC-helix by forming the H-bond network and hydrophobic interactions (Figure 5A). The main chains of Phe811 and Gly812 of the DFG motif on the A-loop form H-bonds with the side chains of Glu640 and Ser639 in αC-helix, respectively, while the side chain of Phe811 forms hydrophobic interactions with Val643, Lue644, and Leu647 in αC-helix (Figure 5A). In comparison, binding of **10a** flipped the DFG motif to an out conformation and also induced a conformational change of A-loop (Figure 4B), resulting in a loss of the interactions with αC-helix (Figure 5B). Instead of stabilizing the A-loop, the Glu640 of the αC-helix formed extensive H-bond interactions with the urea moiety of **10a**. In addition, the Phe811 of the A-loop moved away from the αC-helix and formed strong "edge-to-face" aromatic interactions with the phenyl ring of **10a** (Figure 5B).

Significant structural differences between the activated c-KIT and activated c-KIT/**10a** were observed in the JM domain. Residue Tyr568 and Tyr570 in the JM domain are two important phosphorylation sites at the early stage of c-KIT activation.[8] Upon phosphorylation of Tyr570, critical interactions are formed between the JM domain and the activated A-loop (Figure 5C). In addition to an H-bond interaction between Asn819 in the A-loop and main chain of p-Tyr570, the salt bridge between the ε-NH_3^+ group of Lys818 in the A-loop and the phosphate group of p-Tyr570, as well as hydrophobic interaction between these two lateral side chains, provide a strong and specific force tethering these two domains (Figure 5C). However, binding of **10a** induced a movement of αC-helix and concurrently resulted in the rearrangement of the JM domain (Figure 5D). The movement of αC-helix shifted the Ser639 and consequently deprived the interaction network between Ser639 and the DFG motif (Figure 5D). More importantly, due to the movement of the αC-helix, Met638 was observed to cause a steric clash with the Tyr578 of the JM domain (Figure 5D). In addition, the side chain of Lys642 on the αC-helix shifted to a new orientation, which consequently disrupted its original H-bond interaction with Pro577 (Figure 5C) and formed a new interaction with Thr574 of the JM domain (Figure 5D). These initiated conformational changes of the JM domain, and the p-Tyr570 of the redirected JM domain no longer interacted with and stabilized the A-loop. The movement of JM domain was further accomplished by formation of new interaction network (Figure 5D). The p-Tyr570 and Ile571 formed new H-bond interactions with residues Phe848, Glu849 and Asn787 at the C-lobe (Figure 5D, red dash line). In addition to H-bonds, the p-Tyr570 and Ile571 also formed hydrophobic interactions with Phe848 and Ile789, and with Cys788, respectively (Figure 5D, gray dash line). These strong H-bond interactions and extensive hydrophobic interactions stabilized JM domain in the space that was previously occupied by the activated A-loop (Figure 6, blue arrow), which led to a full detachment of the A-loop from its activated composition. Consequently, the destabilized and detached A-loop can be leveraged back and stabilized by **10a** in a DFG-out inactive conformation (Figure 6, yellow arrow). Taken together, our results constituted the first structural insights into the mechanism underlying actions of a small molecule inhibiting the activated c-KIT.

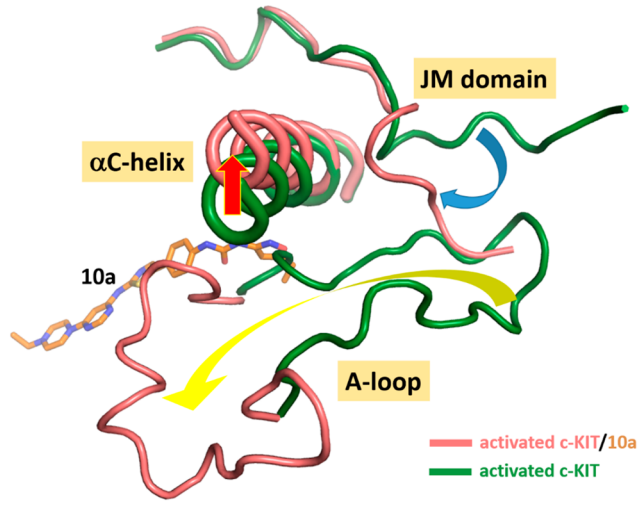

Figure 6. Compound **10a** switched the activated c-KIT back to the inactive state. Upon binding of **10a** (orange) to the activated c-KIT (green) (PDB 1PKG), the αC-helix shifted (red arrow) and the JM domain (pink) repositioned (blue arrow) (PDB 6ITV) to the space that was previously occupied by the activated A-loop (green). The A-loop (pink), therefore, was detached and switched back to the inactive conformation (yellow arrow).

Compound 10a Inhibits Enzymatic Activities of a Broad Spectrum of c-KIT Mutants. The ability of **10a** to potently inhibit activated c-KIT suggested to us that **10a** would also inhibit c-KIT mutants that are constitutively activated. Accordingly, various single- or double-mutant isoforms of c-KIT were evaluated for their susceptibility to inhibition by **10a**. As shown in Table 3, compound **10a** more effectively inhibited a broad spectrum of c-KIT mutants bearing single mutations in the JM domain, ATP-binding pocket and the A-loop than sunitinib. In addition to single c-KIT mutants, **10a** also potently inhibited c-KIT double mutants containing primary V560G and secondary mutations at the A-loop (D816V and N822K), although reduced potency was observed in the V559D/V654A double mutant (Table 3). The reduced potency observed in the V559D/V654A double mutant was investigated by the modeling study. Unlike the extensive hydrophobic network formed between Val654, **10a**, and the surrounding residues Cys809 and Leu799 (Supporting Information, Figure S4A), mutation of Val654 to Ala654 loses the hydrophobic interactions with **10a** as well as with the surrounding residues Cys809 and Leu799 (Supporting Information, Figure S4B). As for Val559, the other mutated residue in the c-KIT double mutant (V559D/V654A), the structural explanation of how it affects the affinity of **10a** is uncertain because it locates in a flexible region that is unobservable in our crystal structure.

DOI: 10.1021/acs.jmedchem.8b01845
J. Med. Chem. XXXX, XXX, XXX−XXX

Table 3. Inhibition of Enzymatic Activities of c-KIT Mutants by 10a or Sunitinib (by HotSpot Kinase Profiling, Reaction Biology Corporation)

mutant forms of c-KIT			% inhibition of enzymatic activities				IC_{50}(nM)
			10a		sunitinib		10a
			100 nM	10 nM	100 nM	10 nM	
JM domain	Exon 11	V560G	99	95	41	8	0.98
ATP binding pocket	Exon 13	V654A	75	43	73	48	4.14
	Exon 13	K642E	99	82	80	60	1.37
	Exon 14	T670I	83	55	93	43	1.66
A-loop	Exon 17	D816H	96	73	56	12	0.67
	Exon 17	D816V	73	37	47	5	8.56
	Exon 17	D820E	100	83	65	16	0.81
	Exon 17	D820Y	100	99	81	36	0.02
	Exon 17	Y823D	100	97	85	28	0.12
	Exon 18	A829P	99	90	43	6	0.89
double mutant	Exon 11/13	V559D/V654A	43	10	82	32	102.0
	Exon 11/17	V560G/D816V	63	22	52	9	9.27
	Exon 11/17	V560G/N822K	99	94	51	7	0.18

In conclusion, **10a** inhibits not only the activated form of c-KIT, but also a broad range of c-KIT mutants including those notoriously resistant to sunitinib treatment at the A-loop.[39,24]

In addition to c-KIT, the ability of **10a** to inhibit other kinases was also investigated. **10a** was profiled over a panel of 468 kinases. The TREEsport interactions maps and the selectivity score of **10a** are shown in Supporting Information, Figure S5.

Antiproliferative Effects of 10a on c-KIT Mutant GIST Cell Lines. To investigate the inhibitory properties of **10a** at a cellular level, its antiproliferative activities against GIST cell lines were evaluated. Three GIST cell lines, GIST882 cells carrying a *c-KIT* exon 13 mutation encoding K642E, GIST430 cells harboring a primary *c-KIT* exon 11 in-frame deletion and a heterozygous secondary exon 13 missense mutation encoding V654A, and GIST48 cells containing a homozygous exon 11 missense mutation encoding V560D and a heterozygous secondary exon 17 mutation encoding D820A were investigated. Compound **10a** showed superior antiproliferative activities against all the three GIST cell lines, GIST882, GIST430, and GIST48, with GI_{50} values of 3, 1, and 2 nM, respectively (Table 4). Consistent with the previous studies,[40] imatinib showed activity in GIST882 cells but was ineffective in GIST430 and GIST48 cells, whereas treatment with sunitinib had an antiproliferative effect on GIST882 and GIST430 cells but not GIST48 cells (Table 4).

Moreover, the inhibition effect of **10a** on c-KIT independent GIST cell lines, GIST48B and GIST62, was evaluated (Supporting Information, Figure S6). The GI_{50} value of **10a** is >100 nM in both c-KIT independent GIST cell lines, suggesting that **10a** exhibited inhibition selectivity between the c-KIT driven GIST cell lines and c-KIT independent GIST cell lines.

In addition, the inhibition effect of **10a** on other cancer cell lines and normal cell line was also evaluated (Supporting Information, Figure S7). The GI_{50} of **10a** in PC3 (human prostate cancer cell line) and A549 (human nonsmall-cell lung cancer cell line) are >20 and 14.6 μM, respectively. Moreover, **10a** had no inhibition effect on Detroit 551 (normal human skin fibroblast cell), with GI_{50} > 10 μM.

Furthermore, the effect of **10a** on the c-KIT-mediated signaling pathway was investigated. As shown in Figure 7, **10a** inhibits c-KIT phosphorylation and the phosphorylation of its downstream signaling molecules, such as AKT, MEK, and MAPK, confirming the on-target effect of **10a**.

Table 4. Inhibitory Activity of Imatinib, Sunitinibband 10a against GIST Cell Lines

cell line	primary/secondary mutation	GI_{50} (nM)[a]		
		imatinib	sunitinib	10a
GIST882	K642E/none	195	64	3
GIST430	V560-L576del/V654A	929	47	1
GIST48	V560D/D820A	625	2000	2

[a]Values of GI_{50} are expressed as the mean of three independent experiments.

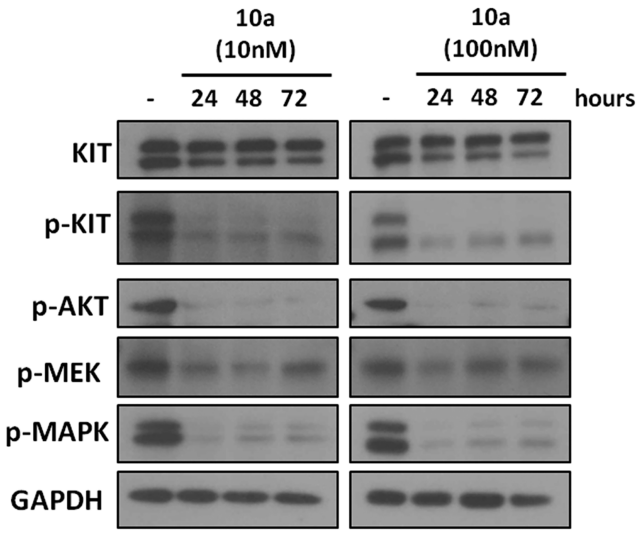

Figure 7. Inhibition effect of compound **10a** on the phosphorylation of c-KIT and its downstream signaling molecules in GIST430.

DOI: 10.1021/acs.jmedchem.8b01845
J. Med. Chem. XXXX, XXX, XXX−XXX

Pharmacokinetics, Pharmacodynamics, and in Vivo Efficacy. The pharmacokinetic properties of **10a** were evaluated using a mouse model. In ICR mice, intravenous administration of **10a** at a dosage of 2 mg/kg gave rise to high volume of distribution (V_{ss} = 7.1 L/kg) and plasma clearance rate (Cl = 20.2 mL/min/kg). Oral administration of **10a** in water solution containing 20% hydroxypropyl-β-cyclodextrin with dosage of 10 mg/kg revealed a short half-life ($t_{1/2}$ = 2.8 h), moderate C_{max} (562 ng/mL) and AUC (2796 ng/mL·h), and 38% of bioavailability.

The pharmacodynamic study of **10a** was also performed. Pharmacodynamic analysis of tumor in GIST430 xenografts harvested 8 h after **10a** administration revealed that decreased c-KIT phosphorylation (p-c-KIT) in a dose-dependent response was observed in mice treated with **10a** compared with those in the controls, demonstrating the on-target effect of **10a** on c-KIT inhibition in vivo. **10a** at a 20 mg/kg dose resulted in 85% p-c-KIT inhibition. while **10a** at a 80 mg/kg dose resulted in 95.9% p-c-KIT inhibition (Supporting Information, Figure S8).

On the basis of the excellent cellular potency and these favorable pharmacokinetic properties and pharmacodynamic results, the antitumor efficacy of **10a** was further investigated in the GIST430 tumor xenograft model (Figure 8). NOD-SCID mice were implanted subcutaneously (SC) with GIST430 tumor cells, and treatment with either sunitinib or **10a** was initiated when tumors reached an average volume of 155 mm^3 at an oral dose of 40 or 25 mg/kg, respectively, on days 1−5 and 8−12. The antitumor growth effect of **10a** is superior to sunitinib (Figure 8). Compound **10a** not only inhibited tumor growth throughout the dosing period, but also reduced tumor size by 59% on day 14. In comparison, treatment of sunitinib only inhibited tumor growth, but no obvious tumor regression was observed.

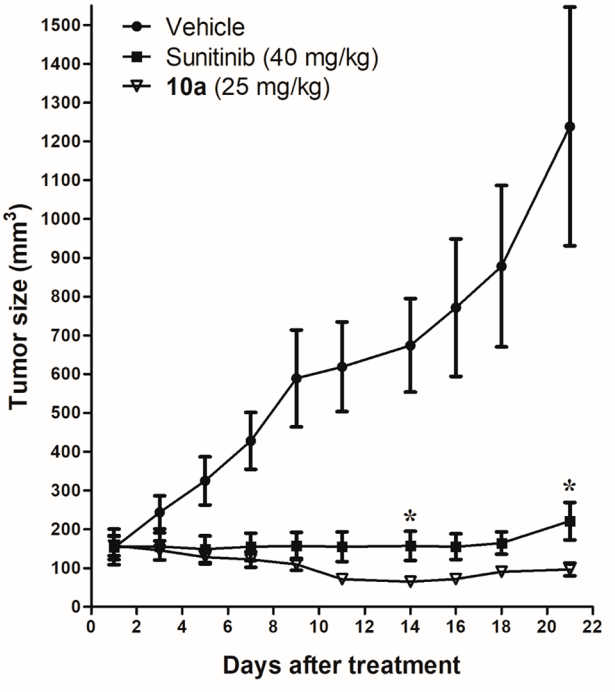

Figure 8. Comparison of antitumor efficacy of **10a** and sunitinib in GIST430 xenograft mouse models. After the average size of the tumors reached 155 nm^3, mice were dosed with **10a** orsunitinib (5 days on/2 days off schedule for 2 weeks) by oral gavage. Tumor sizes are expressed as the mean ± SEM (n = 6/group). Mean differences between **10a** and sunitinib treatments at day 14 and 21 were analyzed using Wilcoxon rank sum test. *, $p < 0.05$

DISCUSSION AND CONCLUSIONS

Tumor recurrence due to emergence of imatinib-resistant secondary mutations in *c-KIT* is an ongoing challenge in the treatment of GISTs. The aim of this study is to discover a more promising inhibitor to fill the gap that current inhibitors leave in full coverage of known c-KIT mutants, especially those arising at the A-loop region, in hopes to reach better clinical benefits. Using 5-phenyl-thiazol-2-ylamine as a core structure, **10a** was identified as a potent inhibitor that effectively inhibits c-KIT (Table 1) and a broad spectrum of clinically relevant c-KIT mutants (Table 3). The inhibitory potency of **10a** against c-KIT A-loop mutants is significantly greater than that of sunitinib (Table 3). Consistent with the enzymatic results, **10a** had a promising antiproliferative effect on GIST cell lines (Table 4) and induced tumor regression in the xenograft mouse model (Figure 8). More importantly, our crystal structure results demonstrated that **10a** not only tightly binds to the unactivated c-KIT as a type II inhibitor (Figure 1), it also induces a serial conformational changes that switch the activated c-KIT back to its inactive state (Figures 4−6). Upon binding of **10a**, the urea moiety forms new interactions with αC-helix and the DFG motif, and rearranges them to compositions that facilitate the movement of the JM domain and the final switch of the A-loop into the inactive conformation. The ability of **10a** to switch off the active conformation of c-KIT is consistent with the observation of high potency of **10a** against the activated c-KIT in the enzymatic activity (Figure 3). The structure insights of the conformational changes upon binding of **10a** to the activated c-KIT also rationalize the crosstalk between the JM domain and A-loop in regulation of c-KIT activation. Perturbation of the interaction between the activated JM domain and A-loop, as well as induction of the JM domain into a position that displaces the A-loop in its active conformation, switch c-KIT from active to inactive state in the c-KIT activation equilibrium. Taken together, the excellent biological activities of **10a** and the accompanying structural rationale establish **10a** as a potential drug candidate worthy of clinical evaluation in patients with advanced GISTs.

EXPERIMENTAL SECTION

Chemistry Methods. All commercial chemicals and solvents are reagent grade and were used without further treatment unless otherwise noted. ^{1}H NMR spectra were obtained with a Varian Mercury-300 or a Varian Mercury-400 spectrometer. Chemical shifts were recorded in parts per million (ppm, δ) and were reported relative to the solvent peak or TMS. LC/MS data were measured on an Agilent MSD-1100 ESI-MS/MS system. High-resolution mass spectra (HRMS) were measured with a Thermo Finnigan (TSQ Quantum) electrospray ionization (ESI) mass spectrometer. Flash column chromatography was done using silica gel (Merck Kieselgel 60, no. 9385, 230−400 mesh ASTM). Reactions were monitored by TLC using Merck 60 F_{254} silica gel glass backed plates (5 cm × 10 cm); zones were detected visually under ultraviolet irradiation (254 nm) or by spraying with phosphomolybdic acid reagent (Aldrich), followed by heating at 80 °C. All starting materials and amines were commercially available unless otherwise indicated. The purity of target compounds was determined with a Hitachi 2000 series HPLC system based on reverse phase C_{18} column (Agilent ZORBAX Eclipse XDB-

DOI: 10.1021/acs.jmedchem.8b01845
J. Med. Chem. XXXX, XXX, XXX−XXX

C18 5 μm, 4.6 mm × 150 mm) under the following gradient elution condition: Mobile phase A-acetonitrile (10% to 90%, 0 to 45 min) and mobile phase B-10 mM NH_4OAc aqueous solution containing 0.1% formic acid (90% to 10%, 0−45 min). The flow-rate was 0.5 mL/min and the injection volume was 20 μL. The system operated at 25 °C. Peaks were detected at λ = 254 nm. The purity of all tested compounds is ≥95% purity except for compounds **10f** (93.8%), **10j** (94.0%), and **11** (93.9%).

Compounds **10**−**11** were prepared following the previous publication with some modifications.[33]

*1-(5-Ethylisoxazol-3-yl)-3-(4-{2-[6-(4-ethylpiperazin-1-yl)-pyrimidin-4-ylamino]thiazol-5-yl}phenyl)urea HCl Salt (**10a**).* Melting point 276−277 °C. ^{1}H NMR (400 MHz, DDMSO-d_6): δ 11.24 (bs, 1H), 9.81 (s, 1H), 9.71 (s, 1H), 8.50 (s, 1H), 7.76 (s, 1H), 7.55−7.49 (m,4H), 6.56 (s, 1H), 6.42 (s, 1H), 4.36 (d, *J* = 13.2 Hz, 2H), 3.57 (d, *J* = 11.6 Hz, 2H), 3.45 (t, *J* = 12.4 Hz, 2H), 3.17−3.01 (m, 4H), 2.71 (q, *J* = 7.6 Hz, 2H), 1.28 (t, *J* = 7.2 Hz, 3H), 1.21 (t, *J* = 7.6 Hz, 3H). MS (ES$^+$) *m*/*z* calcd for $C_{25}H_{29}N_9O_2S$ 519.22, found 520.2 (M + H$^+$). HRMS (ESI) calcd for $C_{25}H_{30}N_9O_2S$ 520.2243, found 520.2241 (M + H$^+$).

*1-(5-Ethyl-3-isoxazolyl)-3-[4-(2-[6-(4-ethylpiperazino)-2-methyl-4-pyrimidinyl]amino-1,3-thiazol-5-yl)phenyl]urea HCl Salt (**10b**).* Melting point 259−260 °C. ^{1}H NMR (400 MHz, DMSO-d_6): δ 11.12 (s, 1H), 9.48 (s, 1H), 8.95 (s, 1H), 7.66 (s, 1H), 7.48 (ABq, $\Delta\nu_{AB}$ = 16.4 Hz, J_{AB} = 8.8 Hz, 4H), 6.55 (s, 1H), 6.05 (s, 1H), 3.50 (br s, 4H), 2.70 (q, *J* = 7.6 Hz, 2H), 2.41−2.32 (m, 9H), 1.22 (t, *J* = 7.6 Hz, 3H), 1.03 (t, *J* = 7.2 Hz, 3H). MS (ES+) *m*/*z* calcd for $C_{26}H_{31}N_9O_2S$: 533.23, found 534.2 (M + H$^+$). HRMS (ESI) calcd for $C_{26}H_{32}N_9O_2S$ 534.2400, found 534.2390 (M + H$^+$).

*1-[4-(2-{[2-Methyl-6-(4-methylpiperazin-1-yl)pyrimidin-4-yl]-amino}-1,3-thiazol-5-yl)phenyl]-3-phenylurea (**10c**).* Melting point 252−253 °C (HCl salt). ^{1}H NMR (300 MHz, DMSO-d_6): δ 11.11 (s, 1H), 8.77 (s, 1H), 8.67 (s, 1H), 7.64 (s, 1H), 7.49−7.44 (m, 6H), 7.28 (t, *J* = 7.8 Hz, 2H), 6.97 (t, *J* = 7.2 Hz, 1H), 6.05 (s, 1H), 3.50 (br s, 4H), 2.41−2.34 (m,7H), 2.22 (s, 3H). MS (ES$^+$) *m*/*z* calcd for $C_{26}H_{28}N_8OS$ 500.63, found 501.47 (M + H$^+$). HRMS (ESI) calcd for $C_{26}H_{29}N_8OS$ 501.2185, found 501.2178 (M + H$^+$).

*(4-{2-[6-(4-Ethylpiperazin-1-yl)pyrimidin-4-ylamino]thiazol-5-ylphenyl)urea HCl Salt (**10d**).* A solution of potassium cyanate (41 mg, 0.5 mmol) in water (1 mL) was added dropwise to a solution of **8** (95 mg, 0.25 mmol) in glacial acetic acid (4 mL) at room temperature. After the reaction mixture was stirred for 30 min, most of solvent was removed under reduced pressure, and the residue was washed with saturated $NaHCO_3$ solution (5 mL). The precipitate was collected by filtration, washed with acetic acid (2 mL), and dried in vacuo. The residue was purified by chromatography on silica gel (10% MeOH/CH_2Cl_2) to give the desired product **10d** as an off-white solid (87 mg, 82%). The above white solid **10d** was added to a stirred solution of 6 N HCl (1 mL) at 0 °C. The solution was filtered through a 0.45 μm PVDF membrane, and the filtrate was collected. Acetone (10 mL) was added to the stirred filtrate dropwise over 1 h. Stirring was continued for an additional 1 h at 0 °C. The precipitate was collected by filtration, washed with acetone (10 mL), and dried in vacuo to give the desired **10d** HCl salt as a yellow solid (102 mg, 99%). ^{1}H NMR (400 MHz, DMSO-d_6): δ 11.05 (s, 1H), 8.89 (s, 1H), 8.46 (s, 1H), 7.67 (s, 1H), 7.43−7.40 (m, 4H), 6.36 (s, 1H), 4.34 (d, *J* = 12.8 Hz, 2H), 3.55 (d, *J* = 11.6 Hz, 2H), 3.39 (t, *J* = 12.6 Hz, 2H), 3.15−3.08 (m, 2H), 3.01 (t, *J* = 10.8 Hz, 2H), 1.25 (t, *J* = 7.2 Hz, 3H). MS (ES$^+$) *m*/*z* calcd for $C_{20}H_{24}N_8OS$ 424.18, found 425.4 (M + H$^+$). HRMS (ESI) calcd for $C_{20}H_{25}N_8OS$ 425.1872, found 425.1867 (M + H$^+$).

*N-[4-(2-{[6-(4-Ethylpiperazin-1-yl)-2-methylpyrimidin-4-yl]-amino}-1,3-thiazol-5-yl)phenyl]benzenesulfonamide (**10e**).* To a solution of **8** (1.0 equiv) in pyridine at room temperature was added benzenesulfonyl chloride (1.1 equiv). After 2 h of stirring at room temperature, the reaction mixture was evaporated to dryness. The residue was suspended in saturated $NaHCO_3$ solution, and the resulting suspension was vigorously stirred at room temperature for 1 h. The resultant solid was collected by filtration and recrystallized from EtOAc/CH_3OH to yield **10e**. Melting point 281−282 °C. ^{1}H NMR (300 MHz, DMSO-d_6): δ 11.13 (s, 1H), 10.35 (s, 1H), 7.79−7.76 (d, *J* = 8.1 Hz, 2H), 7.63−7.53 (m, 4H), 7.44 (d, *J* = 8.7 Hz, 2H), 7.11 (d, *J* = 8.7 Hz, 2H), 5.76 (s, 1H), 4.08 (br s, 1H), 3.33 (s, 1H), 3.16 (d, *J* = 5.4 Hz, 2H), 2.41−2.32 (m, 9H), 1.02 (t, *J* = 7.2 Hz, 3H). MS (ES$^+$) *m*/*z* calcd for $C_{26}H_{29}N_7O_2S_2$ 535.68, found 536.2 (M + H$^+$). HRMS (ESI) calcd for $C_{26}H_{30}N_7O_2S_2$ 536.1902, found 536.1902 (M + H$^+$).

*N-(4-{2-[6-(4-Ethylpiperazin-1-yl)pyrimidin-4-ylamino]thiazol-5-yl}phenyl)acetamide HCl Salt (**10f**).* Melting point 312−313 °C. ^{1}H NMR (400 MHz, D_2O): δ 8.15 (s, 1H), 7.36 (s, 1H), 7.27 (d, *J* = 8.4 Hz, 2H), 7.20 (d, *J* = 8.4 Hz, 2H), 5.92 (s, 1H), 4.28 (d, *J* = 13.6 Hz, 2H), 3.61 (d, *J* = 11.6 Hz, 2H), 3.18 (q, *J* = 7.3 Hz, 4H), 2.89 (d, *J* = 10.8 Hz, 2H), 2.05 (s, 3H), 1.30 (t, *J* = 7.4 Hz, 3H). MS (ES$^+$) *m*/*z* calcd for $C_{21}H_{25}N_7OS$ 423.18, found 424.4 (M + H$^+$). HRMS (ESI) calcd for $C_{21}H_{26}N_7OS$ 424.1920, found 424.1916 (M + H$^+$). HPLC t_R = 11.81 min, 93.8%.

*1-(5-Ethylisoxazol-3-yl)-3-(5-{2-[6-(4-ethylpiperazin-1-yl)-pyrimidin-4-ylamino]thiazol-5-yl}pyridin-2-yl)urea HCl Salt (**10g**).* Melting point 243−244 °C. ^{1}H NMR (400 MHz, DMSO-d_6): δ 11.26 (bs, 1H), 10.76 (bs, 1H), 9.91 (s, 1H), 8.55 (s, 1H), 8.48 (s, 1H), 8.03 (d, *J* = 8.8 Hz, 1H), 7.56 (s, 1H), 7.70 (d, *J* = 8.8 Hz, 1H), 6.60 (s, 1H), 6.39 (s, 1H), 4.37 (d, 2H, overing water peak), 3.56 (d, *J* = 12.0 Hz, 2H), 3.44 (t, *J* = 12.4 Hz, 2H), 3.13 (t, *J* = 6.2 Hz, 2H), 3.02 (q, *J* = 10.0 Hz, 2H), 2.73 (q, *J* = 7.6 Hz, 2H), 1.27 (t, *J* = 7.2 Hz, 3H), 1.22 (t, *J* = 7.6 Hz, 3H), MS (ES$^+$) *m*/*z* calcd for $C_{24}H_{28}N_{10}O_2S$ 520.21, found 521.2 (M + H$^+$). HRMS (ESI) calcd for $C_{24}H_{29}N_{10}O_2S$ 521.2196, found 521.2189 (M + H$^+$).

*1-(5-Ethylisoxazol-3-yl)-3-(4-{2-[6-(4-ethylpiperazin-1-yl)-pyrimidin-4-ylamino]-4-methylthiazol-5-yl}phenyl)urea HCl Salt (**10h**).* Melting point 275−276 °C. ^{1}H NMR (400 MHz, DMSO-d_6): δ 11.08 (bs, 1H), 9.76 (s, 1H), 9.58 (s, 1H), 8.47 (s, 1H), 7.54 (d, *J* = 8.0 Hz, 2H), 7.40 (d, *J* = 8.0 Hz, 2H), 6.56 (s, 1H), 6.38 (s, 1H), 4.36 (d, *J* = 10.8 Hz, 2H), 3.56 (d, *J* = 11.6 Hz, 2H), 3.42 (t, *J* = 12.4 Hz, 2H), 3.13−3.01 (m, 4H), 2.71 (q, *J* = 7.2 Hz, 4H), 2.34 (s, 3H), 1.28 (t, *J* = 6.4 Hz, 3H), 1.21 (t, *J* = 7.2 Hz, 3H). MS (ES$^+$) *m*/*z* calcd for $C_{26}H_{31}N_9O_2S$ 533.23, found 534.2 (M + H$^+$). HRMS (ESI) calcd for $C_{26}H_{32}N_9O_2S$ 534.2400, found 534.2383 (M + H$^+$).

*1-(5-Ethylisoxazol-3-yl)-3-(4-{2-[4-(4-ethylpiperazin-1-yl)-6-methyl-[1,3,5]triazin-2-ylamino]thiazol-5-yl}phenyl)urea HCl Salt (**10i**).* Melting point 277−278 °C. ^{1}H NMR (400 MHz, DMSO-d_6): δ 11.32 (br, 1H), 9.77 (d, *J* = 8.8 Hz, 1H), 9.63 (d, *J* = 19.6 Hz, 1H), 8.13 (d, *J* = 10.0 Hz, 1H), 7.58 (dd, *J* = 29.2, 7.6 Hz, 4H), 6.55 (s, 1H), 4.83 (d, *J* = 14.0 Hz, 1H), 3.80 (br, 2H), 3.59 (d, *J* = 10.0 Hz, 2H), 3.16−3.08 (m, 4H), 2.72 (t, *J* = 15.2, 7.6 Hz, 3H), 2.39 (s, 2H), 1.30 (t, *J* = 7.2 Hz, 3H), 1.21 (t, *J* = 7.6 Hz, 3H). MS (ES$^+$) *m*/*z* calcd for $C_{25}H_{30}N_{10}O_2S$ 534.2, found 535.2 (M + H$^+$). HRMS (ESI) calcd for $C_{25}H_{31}N_{10}O_2S$ 535.2352, found 535.2341 (M + H$^+$).

*1-(5-Ethylisoxazol-3-yl)-3-[4-(2-{6-[4-(2-hydroxyethyl)piperazin-1-yl]-pyrimidin-4-ylamino}thiazol-5-yl)phenyl]urea Dihydrochloride (**10j**).* Melting point 272−273 °C. ^{1}H NMR (400 MHz, DMSO-d_6): δ 10.77 (bs, 1H), 9.79 (s, 1H), 9.66 (s, 1H), 8.49 (s, 1H), 7.74 (s, 1H), 7.55−7.49 (m, 4H), 6.56 (s, 1H), 6.40 (s, 1H), 4.34 (d, *J* = 13.2 Hz, 2H), 3.81 (t, *J* = 5.0 Hz, 2H), 3.62 (d, *J* = 12.0 Hz, 2H), 3.45 (t, *J* = 12.4 Hz, 2H), 3.22−3.13 (m, 4H), 2.71 (q, *J* = 7.6 Hz, 4H), 1.21 (t, *J* = 7.6 Hz, 3H). MS (ES$^+$) *m*/*z* calcd for $C_{25}H_{29}N_9O_3S$ 535.21, found 536.2 (M + H$^+$). HRMS (ESI) calcd for $C_{25}H_{30}N_9O_3S$ 536.2192, found 536.2170 (M + H$^+$). HPLC t_R = 14.61 min, 94.0%.

*N-[4-(2-[6-(3-Aminotetrahydro-1H-1-pyrrolyl)-2-methyl-4-pyrimidinyl]amino-1,3-thiazol-5-yl)phenyl]-N′-(5-ethyl-3-isoxazolyl)urea Dihydrochloride (**10k**).* Melting point 267−268 °C. ^{1}H NMR (400 MHz, DMSO-d_6): δ 8.94 (s, 1H), 7.63 (s, 1H), 7.48 (ABq, $\Delta\nu_{AB}$ = 14.0 Hz, J_{AB} = 8.4 Hz, 4H), 6.53 (s, 1H), 5.73 (s, 1H), 3.37 (br s, 7H, overlapping with water peak), 2.69 (q, *J* = 7.2 Hz, 2H), 2.37 (s, 3H), 1.99 (br s, 1H), 1.67 (br s, 1H), 1.19 (t, *J* = 7.6 Hz, 3H). MS (ES$^+$) *m*/*z* calcd for $C_{24}H_{27}N_9O_2S$ 505.20, found 506.2 (M + H$^+$). HRMS (ESI) calcd for $C_{24}H_{28}N_9O_2S$ 506.2087, found 506.2083 (M + H$^+$).

*1-(5-Ethylisoxazol-3-yl)-3-(4-{2-[6-(4-ethylpiperazin-1-yl)-2-methylpyrimidin-4-ylamino]thiazol-4-yl}phenyl)urea HCl Salt (**11**).* Melting point 258−259 °C. ^{1}H NMR (400 MHz, DMSO-d_6): δ 11.21

DOI: 10.1021/acs.jmedchem.8b01845
J. Med. Chem. XXXX, XXX, XXX−XXX

(bs, 1H), 9.83 (s, 1H), 9.72 (s, 1H), 7.81 (d, J = 8.4, 2H), 7.51 (d, J = 8.4, 2H), 7.43 (s, 1H), 6.55 (s, 1H), 6.34 (bs, 1H), 4.37 (d, J = 13.6 Hz, 2H), 3.57−3.41 (m, 4H), 3.14−3.01 (m, 4H), 2.70 (q, J = 7.6 Hz, 2H), 2.45 (s, 3H), 1.27 (t, J = 7.2 Hz, 3H), 1.20 (t, J = 7.6 Hz, 3H). MS (ES^+) m/z calcd for $C_{27}H_{33}N_9O_2S$ 533.23, found 534.1 (M + H^+). HRMS (ESI) calcd for $C_{27}H_{34}N_9O_2S$ 534.2400, found 534.2350 (M + H^+). HPLC t_R = 22.74 min, 93.9%.

*Synthetic Procedure for the Preparation of Urea Analogues **18**, **22**, and **24**.* Sodium hydride (1.6 g, 60% in oil, 39.94 mmol) was added to a solution of 2-aminothiazole **12** (2.0 g, 19.97 mmol) in anhydrous THF (100 mL) at room temperature. After the reaction mixture was stirred for 10 min, a solution of 4,6-dichloro-2-methylpyrimidine **5b** (R = CH_3, 4.9 g, 29.96 mmol) in anhydrous THF (50 mL) was added dropwise and the mixture was stirred overnight. The reaction was quenched by the addition of saturated NH_4Cl solution, and most of solvent was removed under reduced pressure. The residue was stirred vigorously in saturated $NaHCO_3$ solution (250 mL) for 1 h. The precipitate was collected by filtration, washed with water (2 × 30 mL), and purified by chromatography on silica gel (5% MeOH/CH_2Cl_2) to give the desired product **13b** as an off-white solid (3.5 g, 78%).

*(6-Chloro-2-methylpyrimidin-4-yl)thiazol-2-yl-amine (**13b**, R = CH_3).* ^{1}H NMR (400 MHz, DMSO-d_6): δ 11.87 (s, 1H), 7.48 (d, J = 3.6 Hz, 1H), 7.23 (d, J = 3.6 Hz, 1H), 6.92 (s, 1H), 2.55 (s, 3H). MS (ES^+) m/z calcd for $C_8H_7ClN_4S$ 226.01, found 227.0 (M + H^+). A mixture of **13b** (2.0 g, 8.82 mmol) and 1-ethylpiperazine (2.0 g, 17.51 mmol) in pyridine (15 mL) was heated at 65 °C overnight. After cooling to room temperature, most of solvent was removed under reduced pressure and the residue was purified by chromatography on silica gel (5% MeOH/CH_2Cl_2) to give the desired product **14b** as a brown solid (2.4 g, 89%).

*[6-(4-Ethylpiperazin-1-yl)-2-methylpyrimidin-4-yl]thiazol-2-yl-amine (**14b**, R = CH_3).* ^{1}H NMR (400 MHz, DMSO-d_6): δ 11.02 (s, 1H), 7.33 (d, J = 3.6 Hz, 1H), 7.01 (d, J = 3.6 Hz, 1H), 6.03 (s, 1H), 3.50−3.42 (m, 4H), 2.45−2.28 (m, 9H), 1.01 (t, J = 7.2 Hz, 3H). MS (ES^+) m/z calcd for $C_{14}H_{20}N_6S$ 304.15, found 305.1 (M + H^+). A mixture of **14b** (745 mg, 2.45 mmol) and *N*-iodosuccinimide (580 mg, 2.58 mmol) in $CHCl_3$ (20 mL) was stirred at room temperature for 2 h. The reaction was quenched by the addition of saturated sodium thiosulfate solution (5 mL), and the product was extracted with CH_2Cl_2 (2 × 20 mL). The combined organic extract was dried over $MgSO_4$ and concentrated under reduced pressure. The residue was purified by chromatography on silica gel (7% MeOH/CH_2Cl_2) to give the desired product **15b** as a white solid (843 mg, 80%).

*[6-(4-Ethylpiperazin-1-yl)-2-methylpyrimidin-4-yl]-(5-iodothiazol-2-yl)amine (**15b**, R = CH_3).* ^{1}H NMR (400 MHz, $CDCl_3$): δ 8.90 (bs, 1H), 7.39 (s, 1H), 5.67 (s, 1H), 3.68−3.62 (m, 4H), 2.68−2.55 (m, 4H), 2.50 (s, 3H), 2.47 (q, J = 6.8 Hz, 2H), 1.13 (t, J = 7.0 Hz, 3H). MS (ES^+) m/z calcd for $C_{14}H_{19}IN_6S$ 430.04, found 431.0 (M + H^+). A mixture of **15b** (120 mg, 0.28 mmol), *N*-boc-1,2,3,6-tetrahydropyridine-4-boronic acid pinacol ester **16** (172 mg, 0.56 mmol), $PdCl_2$(dppf) (80 mg, 0.11 mmol), and Na_2CO_3 (1.0 mmol in 0.5 mL of water) in 1,4-dioxane (4 mL) was heated at 80 °C for 2 h. After cooling to room temperature, the reaction mixture was filtered through a short pad of Celite and most of solvent was removed under reduced pressure. The residue was purified by chromatography on silica gel (10% MeOH/CH_2Cl_2) to afford crude Boc-**17** as a brown solid (100 mg). A mixture of Boc-**17** (100 mg, 0.21 mmol) and TFA (1 mL) in CH_2Cl_2 (4 mL) was stirred at room temperature overnight. Most of solvent was removed under reduced pressure, and the residue was purified by chromatography on silica gel (15% MeOH/CH_2Cl_2) to give the desired product **17** as a brown solid (30 mg, 38%).

*[6-(4-Ethylpiperazin-1-yl)-2-methylpyrimidin-4-yl]-[5-(1,2,3,6-tetrahydropyridin-4-yl)thiazol-2-yl]amine (**17**).* ^{1}H NMR (300 MHz, DMSO-d_6): δ 7.24 (s, 1H), 6.03 (s, 1H), 5.89 (s, 1H), 3.55−3.36 (m, 6H, overlapping with water), 2.91 (t, J = 5.6 Hz, 2H), 2.49−2.31 (m, 11H), 0.98 (t, J = 7.1 Hz, 3H). MS (ES^+) m/z calcd for $C_{19}H_{27}N_7S$ 385.20, found 386.2 (M + H^+). 5-Ethylisoxazol-3-yl)carbamic acid 4-nitro-phenyl ester (45 mg, 0.16 mmol) was added to a solution of **17** (30 mg, 0.08 mmol) in pyridine (1 mL) at room temperature, and the mixture was stirred overnight. Most of solvent was removed under reduced pressure, and the residue was purified by chromatography on silica gel (10% MeOH/CH_2Cl_2) to give the desired product **18** as a yellow solid (27 mg, 65%).

*4-{2-[6-(4-Ethylpiperazin-1-yl)-2-methylpyrimidin-4-ylamino]-thiazol-5-yl}-3,6-dihydro-2H-pyridine-1-carboxylic Acid (5-Ethyl-isoxazol-3-yl)amide (**18**).* Melting point 245−246 °C. ^{1}H NMR (300 MHz, DMSO-d_6): δ 11.08 (bs, 1H), 9.68 (s, 1H), 7.32 (s, 1H), 6.49 (s, 1H), 6.04 (s, 1H), 5.90 (bs, 1H), 4.10 (bs, 2H), 3.65 (bs, 2H), 3.55−3.40 (m, 4H), 2.68 (q, J = 7.5 Hz, 2H), 2.41−2.34 (m, 11H, overlapping with DMSO), 1.19 (t, J = 7.5 Hz, 3H), 1.02 (t, J = 7.2 Hz 3H). MS (ES^+) m/z calcd for $C_{25}H_{33}N_9O_2S$ 523.25, found 524.3 (M + H^+). HRMS (ESI) calcd for $C_{25}H_{34}N_9O_2S$ 524.2556, found 524.2552 (M + H^+). A mixture of **15a** (R = H, 200 mg, 0.48 mmol), *N*-propargylphthalimide **19** (178 mg, 0.96 mmol), $Pd(PPh_3)_4$ (58 mg, 0.05 mmol), copper(I) iodide (19 mg, 0.10 mmol), and triethylamine (0.20 mL, 1.44 mmol) in dry THF (5 mL) was stirred at room temperature overnight. The reaction mixture was filtered through a short pad of Celite, and most of the solvent was removed under reduced pressure. The residue was partitioned between water (20 mL) and CH_2Cl_2 (20 mL). The organic layer was separated, and the aqueous layer was extracted with CH_2Cl_2 (2 × 10 mL). The combined organic layer was dried over $MgSO_4$ and concentrated to afford **20a** (R = H) as a brown solid which was used in the next step without further purification (43 mg, 19%). Hydrazinium hydroxide (0.25 mL, 4.8 mmol) was added dropwise to a solution of crude **20a** (43 mg, 0.09 mmol) in THF (5 mL) at 0 °C, and the mixture was stirred at room temperature overnight. The volatiles were removed under reduced pressure, and the residue was partitioned between water (10 mL) and CH_2Cl_2 (20 mL). The organic layer was separated, and the aqueous layer was extracted with CH_2Cl_2 (2 × 20 mL). The combined organic layer was dried over $MgSO_4$ and concentrated. The residue was purified by chromatography on silica gel (10% MeOH/CH_2Cl_2) to give the desired product **21a** (R = H) as a white solid (26 mg, 85%). The same synthetic procedure as **21a** yielded **21b** (R = CH_3) as a white solid (90%).

*[5-(3-Aminoprop-1-ynyl)thiazol-2-yl]-[6-(4-ethylpiperazin-1-yl)-pyrimidin-4-yl]amine (**21a**, R = H).* ^{1}H NMR (400 MHz, $CDCl_3$): δ 8.42 (s, 1H), 7.44 (s, 1H), 5.97 (s, 1H), 3.68−3.65 (m, 6H), 2.54 (t, J = 5.0 Hz, 4H), 2.48 (q, J = 7.2 Hz, 2H), 1.14 (t, J = 7.2 Hz, 3H).

*[5-(3-Aminoprop-1-ynyl)thiazol-2-yl]-[6-(4-ethylpiperazin-1-yl)-2-methylpyrimidin-4-yl]amine (**21b**, R = CH_3).* ^{1}H NMR (400 MHz, DMSO-d_6): δ 7.47 (s, 1H), 5.97 (s, 1H), 3.51 (s, 2H), 3.50−3.44 (m, 4H), 2.42−2.35 (m, 4H), 2.36 (s, 3H), 2.33 (q, J = 7.2 Hz, 2H), 1.01 (t, J = 7.2 Hz, 3H). MS (ES^+) m/z calcd for $C_{17}H_{23}N_7S$ 357.17, found 358.1 (M + H^+). The synthesis of final products **22** from amine **21a** (yield 80%) was the same as that of urea **18** from amine **17**.

*1-(5-Ethylisoxazol-3-yl)-3-(3-{2-[6-(4-ethylpiperazin-1-yl)-pyrimidin-4-ylamino]thiazol-5-yl}prop-2-ynyl)urea (**22**).* ^{1}H NMR (300 MHz, DMSO-d_6): δ 11.48 (s, 1H), 9.50 (s, 1H), 8.34 (s, 1H), 7.56 (s, 1H), 6.91 (t, J = 5.4 Hz, 1H), 6.42 (s, 1H), 6.18 (s, 1H), 4.19 (d, J = 5.4 Hz, 2H), 3.52−3.42 (m, 4H), 2.69 (q, J = 7.2 Hz, 2H), 2.50−2.35 (m, 6H, overlapping with DMSO), 1.19 (t, J = 7.5 Hz, 3H), 1.06 (t, J = 6.9 Hz, 3H). MS (ES^+) m/z calcd for $C_{22}H_{27}N_9O_2S$ 481.2, found 482.2 (M + H^+). HRMS (ESI) calcd for $C_{22}H_{28}N_9O_2S$ 481.2087, found 482.2085 (M + H^+). A mixture of **21b** (50 mg, 0.14 mmol) and Pd/$BaSO_4$ (30 mg)in MeOH (2 mL) was stirred under a hydrogen atmosphere at room temperature overnight. The reaction mixture was filtered through a short pad of Celite, and most of the solvent was removed under reduced pressure. The residue was purified by chromatography on silica gel (15% MeOH/CH_2Cl_2) to give the desired product **23** as a brown solid (29 mg, 57%).

*[5-(3-Aminopropyl)-thiazol-2-yl]-[6-(4-ethylpiperazin-1-yl)-2-methylpyrimidin-4-yl]amine (**23**).* ^{1}H NMR (300 MHz, $CDCl_3$): δ 7.02 (s, 1H), 5.88 (s, 1H), 3.78−3.57 (m, 4H), 2.82−2.74 (m, 4H), 2.54−2.41 (m, 9H), 1.90−1.75 (m, 2H), 1.12 (t, J = 7.2 Hz, 3H). MS (ES^+) m/z calcd for $C_{17}H_{27}N_7S$ 361.2, found 362.2 (M + H^+). The synthesis of final product **24** from amine **23** (yield 90%) was the same as that of urea **18** from amine **17**.

DOI: 10.1021/acs.jmedchem.8b01845
J. Med. Chem. XXXX, XXX, XXX−XXX

*1-(5-Ethylisoxazol-3-yl)-3-(3-{2-[6-(4-ethylpiperazin-1-yl)-2-methylpyrimidin-4-ylamino]thiazol-5-yl}propyl)urea (**24**).* ^{1}H NMR (300 MHz, DMSO-d_6): δ 10.88 (bs, 1H), 9.28 (s, 1H), 7.06 (s, 1H), 6.59 (t, J = 5.4 Hz, 1H), 6.38 (s, 1H), 6.04 (s, 1H), 3.58−3.42 (m, 4H), 3.15 (td, J = 6.3, 5.4 Hz, 2H), 2.73−2.63 (m, 4H), 2.55−2.32 (m, 9H, overlapping with DMSO), 1.82−1.71 (m, 2H), 1.18 (t, J = 7.5 Hz, 3H), 1.03 (t, J = 7.1 Hz, 3H). MS (ES$^+$) m/z calcd for $C_{23}H_{33}N_9O_2S$ 499.25, found 500.2 (M + H$^+$). HRMS (ESI) calcd for $C_{23}H_{34}N_9O_2$: 500.2556, found 500.2551 (M + H$^+$). ^{13}C NMR spectrum of **10a** and HPLC traces of **10a**−**10k**, **11**, **18**, **22**, and **24** are shown in Supporting Information, Figure S9.

Kinase Expression, Purification, and Activation. Human c-KIT kinase was expressed using a baculovirus expression system. Briefly, cDNA encoding c-KIT residues 547−935, with the kinase insertion domain (residues 694−753) being deleted and replaced by a 6-nucleotide fragment encoding Thr-Ser, was cloned. A 6x-histidine tag followed by a thrombin cleavage site was added in-frame to the N-terminus of the cloned *c-KIT*, and the whole fragment was inserted into the pBacPAK8 vector. Recombinant c-KIT was expressed in Sf9 insect cells grown in Grace's insect medium supplemented with 10% fetal bovine serum (FBS) and antibiotics (100 U penicillin/mL and 100 μg streptomycin/mL). Cell pellets were lysed in lysis buffer (25 mM Tris-HCl, pH7.6, 250 mM NaCl, and 0.5 mM TCEP) by sonication. His-tagged c-KIT proteins were affinity purified with HisTrap HP column (GE Life Sciences). Proteins were eluted by a liner imidazole gradient, and the buffer was exchanged to thrombin buffer (20 mM Tris-HCl, pH8.4, 150 mM NaCl, and 2.5 mM $CaCl_2$) for overnight thrombin cleavage at 4 °C. After removal of the histidine tag, the c-KIT proteins were subjected to a buffer exchange to the final buffer containing 25 mM Tris-HCl, pH 7.6, 250 mM NaCl, and 5 mM DTT.

To obtain the activated c-KIT proteins, 10 times in molar ratio of ATP was incubated with c-KIT at room temperature for 2 h, followed by a final concentrating step at 4 °C. To verify the phosphorylation status of the activated c-KIT, Western blotting assays using antiphospho-tyrosine antibodies and Coomassie Brilliant Blue staining of total proteins were performed. As shown in Supporting Information, Figure S1, the purified c-KIT proteins were unphosphorylated (lane 1), indicating that the proteins are in the unactivated state before ATP activation. In contrast, the c-KIT proteins were predominantly phosphorylated in the first hour of ATP incubation (lane 2), and the activation reached to a level that almost all c-KIT proteins were phosphorylated after 2 h of ATP incubation (lane 3).

Crystallization of c-KIT with Compound 10a. Crystallization of the c-KIT kinase domain with **10a** was performed by the hanging drop method. A solution of the unactivated c-KIT (5.0 mg/mL) was preincubated with **10a** (0.6 mM) on ice for 20 min and mixed with an equal volume of reservoir solution (15% PEG3350, 0.1 M sodium citrate tribasic dihydrate, pH 5.6, and 3% ethylene glycol) plus 2% benzamidine hydrochloride as an additive. The activated c-KIT was cocrystallized with **10a** in a similar way except for an extended incubation time up to 1 h on ice and using 3% 1,6-hexanediol as an additive. Crystals were grown at 18 °C and immersed quickly in cryoprotectant (reservoir solutions with addition of 9% glycerol and a mixture of 3% glycerol and 7.5% ethylene glycol for the unactivated and activated c-KIT crystals, respectively) before being flash-frozen in liquid nitrogen. The X-ray diffraction data sets were collected at beamline 15A1 (NSRRC, Taiwan) and beamline 44XU (Spring-8, Japan) and processed using the software program HKL2000 (HKL Research, Inc.). The initial phases of c-KIT kinase domain structures were obtained by molecular replacement in the PHENIX package using the previously reported c-KIT structure (PDB 1T46) as a template. Structure refinement and model building were performed using PHENIX and COOT, and structure results were depicted using PyMOL (Schrödinger, LLC).

Biochemical Kinase Assays. For SAR analysis (Table 1), the enzymatic activities of c-KIT were determined by in vitro kinase assays using the ADP-Glo reagent (Promega) according to manufacturer's instructions. Briefly, 250 ng of c-KIT proteins were incubated with compounds in the 10 μL of reaction buffer (40 mM Tris−HCl, pH 7.4, 2 mM $MnCl_2$, 2 mM DTT, 20 mM $MgCl_2$, 0.1 mg/mL bovine serum albumin, 1 mM Na_3VO_4) containing 20 μM ATP and 40 μM poly(Glu_4-Tyr_1) as substrates at 30 °C for 150 min. The ADP-Glo reagent was then added, and the mixture was incubated at 25 °C for 40 min. The kinase detection reagent was added for another 30 min at 25 °C. The converted ADP was determined by luminescence measurement using the Wallac Vector 1420 multilabel counter (PerkinElmer).

To determine the IC_{50} values of imatinib, sunitinib, or **10a** to the unactivated and activated c-KIT (Figure 3), kinase assays were performed using the Kinase-GloPlus reagents (Promega). Briefly, 250 nM of the unactivated or activated c-KIT proteins were incubated with imatinib, sunitinib, or **10a** in the reaction buffer (40 mM Tris-HCl, pH 7.4, 2 mM $MnCl_2$, 2 mM DTT, 20 mM $MgCl_2$, 0.1 mg/mL bovine serum albumin, 1 mM Na_3VO_4) containing 10 μM poly(Glu_4-Tyr_1) as substrates at room temperature for 30 min. After incubation, 5 μM ATP was added to the unactivated c-KIT or activated c-KIT mixtures and incubated at 37 °C for 120 or 30 min, respectively. The Kinase-Glo Plus reagent was then added, and the amount of remained ATP was determined by luminescence measurement using the Wallac Vector 1420 multilabel counter (PerkinElmer).

■ ASSOCIATED CONTENT

Supporting Information

The Supporting Information is available free of charge on the ACS Publications website at DOI: 10.1021/acs.jmedchem.8b01845.

Material and methods of antiproliferation cellular assays; Western blot analysis, pharmacokinetic studies, in vivo pharmacodynamics, and efficacy studies in GIST430 xenografts model; Coomassie Brilliant Blue staining and Western blot analysis of the unactivated and activated c-KIT; Illustration of possible binding modes of **11** with c-KIT; molecular docking of **10f** with c-KIT; modeling study of **10a** bound to c-KIT V654A; the TREEspot interaction maps and selectivity score of **10a**; cell viability of GIST48B and GIST62 cell lines treated with **10a**; cell viability of PC3, A549, and Detroit 551 cell lines treated with **10a**; pharmacodynamic study of **10a**; ^{13}C NMR spectrum of **10a** and HPLC traces of **10a**−**10k**, **11**, **18**, **22**, and **24** (PDF)

Molecular formula strings (CSV)

Accession Codes

6ITT (unactivated c-KIT/**10a**); 6ITV (activated c-KIT/**10a**). Authors will release the atomic coordinates and experimental data upon article publication.

■ AUTHOR INFORMATION

Corresponding Authors

*For S.Y.W.: phone, +886-37-246-166 ext 35713; fax, + 886-37-586-456; E-mail, suying@nhri.org.tw.

*For W.T.J.: phone, +886-37-246-166 ext 35712; fax, + 886-37-586-456; E-mail, wtjiaang@nhri.org.tw.

ORCID

Su-Ying Wu: 0000-0003-2816-6961

Notes

The authors declare no competing financial interest.

■ ACKNOWLEDGMENTS

We thank the staff of beamlines TPS05A, BL15A1, and BL13B1 at the National Synchrotron Radiation Research Center (NSRRC), Taiwan, and SP44XU at the Spring-8, Japan, for technical assistance. This work was supported by

DOI: 10.1021/acs.jmedchem.8b01845
J. Med. Chem. XXXX, XXX, XXX−XXX

National Health Research Institute, and Ministry of Economic Affairs, Taiwan, R.O.C.

■ ABBREVIATIONS USED

GIST, gastrointestinal stromal tumor; RTK, receptor tyrosine kinase; JM, juxtamembrane; A-loop, activation loop; SCF, stem cell factor; SAR, structure−activity relationships

■ REFERENCES

(1) Hubbard, S. R.; Till, J. H. Protein tyrosine kinase structure and function. *Annu. Rev. Biochem.* **2000**, *69*, 373−398.
(2) Blume-Jensen, P.; Hunter, T. Oncogenic kinase signalling. *Nature* **2001**, *411*, 355−365.
(3) Yarden, Y.; Kuang, W. J.; Yang-Feng, T.; Coussens, L.; Munemitsu, S.; Dull, T. J.; Chen, E.; Schlessinger, J.; Francke, U.; Ullrich, A. Human proto-oncogene c-kit: a new cell surface receptor tyrosine kinase for an unidentified ligand. *EMBO J.* **1987**, *6*, 3341−3351.
(4) Mol, C. D.; Dougan, D. R.; Schneider, T. R.; Skene, R. J.; Kraus, M. L.; Scheibe, D. N.; Snell, G. P.; Zou, H.; Sang, B. C.; Wilson, K. P. Structural basis for the autoinhibition and STI-571 inhibition of c-Kit tyrosine kinase. *J. Biol. Chem.* **2004**, *279*, 31655−31663.
(5) Yuzawa, S.; Opatowsky, Y.; Zhang, Z.; Mandiyan, V.; Lax, I.; Schlessinger, J. Structural basis for activation of the receptor tyrosine kinase KIT by stem cell factor. *Cell* **2007**, *130*, 323−334.
(6) Hubbard, S. R. Juxtamembrane autoinhibition in receptor tyrosine kinases. *Nat. Rev. Mol. Cell Biol.* **2004**, *5*, 464−471.
(7) Mol, C. D.; Lim, K. B.; Sridhar, V.; Zou, H.; Chien, E. Y.; Sang, B. C.; Nowakowski, J.; Kassel, D. B.; Cronin, C. N.; McRee, D. E. Structure of a c-kit product complex reveals the basis for kinase transactivation. *J. Biol. Chem.* **2003**, *278*, 31461−31464.
(8) DiNitto, J. P.; Deshmukh, G. D.; Zhang, Y.; Jacques, S. L.; Coli, R.; Worrall, J. W.; Diehl, W.; English, J. M.; Wu, J. C. Function of activation loop tyrosine phosphorylation in the mechanism of c-Kit auto-activation and its implication in sunitinib resistance. *J. Biochem.* **2010**, *147*, 601−609.
(9) Oppelt, P. J.; Hirbe, A. C.; Van Tine, B. A. Gastrointestinal stromal tumors (GISTs): point mutations matter in management, a review. *J. Gastrointest. Oncol.* **2017**, *8*, 466−473.
(10) Hirota, S.; Isozaki, K.; Moriyama, Y.; Hashimoto, K.; Nishida, T.; Ishiguro, S.; Kawano, K.; Hanada, M.; Kurata, A.; Takeda, M.; Muhammad Tunio, G.; Matsuzawa, Y.; Kanakura, Y.; Shinomura, Y.; Kitamura, Y. Gain-of-function mutations of c-kit in human gastrointestinal stromal tumors. *Science* **1998**, *279*, 577−580.
(11) Kozlowski, M.; Larose, L.; Lee, F.; Le, D. M.; Rottapel, R.; Siminovitch, K. A. SHP-1 binds and negatively modulates the c-Kit receptor by interaction with tyrosine 569 in the c-Kit juxtamembrane domain. *Mol. Cell. Biol.* **1998**, *18*, 2089−2099.
(12) Heinrich, M. C.; Corless, C. L.; Demetri, G. D.; Blanke, C. D.; von Mehren, M.; Joensuu, H.; McGreevey, L. S.; Chen, C. J.; Van den Abbeele, A. D.; Druker, B. J.; Kiese, B.; Eisenberg, B.; Roberts, P. J.; Singer, S.; Fletcher, C. D.; Silberman, S.; Dimitrijevic, S.; Fletcher, J. A. Kinase mutations and imatinib response in patients with metastatic gastrointestinal stromal tumor. *J. Clin. Oncol.* **2003**, *21*, 4342−4349.
(13) Xu, C. W.; Lin, S.; Wang, W. L.; Gao, W. B.; Lv, J. Y.; Gao, J. S.; Zhang, L. Y.; Li, Y.; Wang, L.; Zhang, Y. P.; Tian, Y. W. Analysis of mutation of the c-Kit gene and PDGFRA in gastrointestinal stromal tumors. *Exp. Ther. Med.* **2015**, *10*, 1045−1051.
(14) Demetri, G. D.; von Mehren, M.; Blanke, C. D.; Van den Abbeele, A. D.; Eisenberg, B.; Roberts, P. J.; Heinrich, M. C.; Tuveson, D. A.; Singer, S.; Janicek, M.; Fletcher, J. A.; Silverman, S. G.; Silberman, S. L.; Capdeville, R.; Kiese, B.; Peng, B.; Dimitrijevic, S.; Druker, B. J.; Corless, C.; Fletcher, C. D.; Joensuu, H. Efficacy and safety of imatinib mesylate in advanced gastrointestinal stromal tumors. *N. Engl. J. Med.* **2002**, *347*, 472−480.
(15) Joensuu, H.; Eriksson, M.; Sundby Hall, K.; Reichardt, A.; Hartmann, J. T.; Pink, D.; Ramadori, G.; Hohenberger, P.; Al-Batran, S. E.; Schlemmer, M.; Bauer, S.; Wardelmann, E.; Nilsson, B.; Sihto, H.; Bono, P.; Kallio, R.; Junnila, J.; Alvegard, T.; Reichardt, P. Adjuvant imatinib for high-risk GI stromal tumor: analysis of a randomized trial. *J. Clin. Oncol.* **2016**, *34*, 244−250.
(16) Casali, P. G.; Zalcberg, J.; Le Cesne, A.; Reichardt, P.; Blay, J. Y.; Lindner, L. H.; Judson, I. R.; Schoffski, P.; Leyvraz, S.; Italiano, A.; Grunwald, V.; Pousa, A. L.; Kotasek, D.; Sleijfer, S.; Kerst, J. M.; Rutkowski, P.; Fumagalli, E.; Hogendoorn, P.; Litiere, S.; Marreaud, S.; van der Graaf, W.; Gronchi, A.; Verweij, J. Ten-year progression-free and overall survival in patients with unresectable or metastatic GI stromal tumors: long-term analysis of the European organisation for research and treatment of cancer, Italian sarcoma group, and Australasian gastrointestinal trials group intergroup phase III randomized trial on imatinib at two dose levels. *J. Clin. Oncol.* **2017**, *35*, 1713−1720.
(17) Heinrich, M. C.; Owzar, K.; Corless, C. L.; Hollis, D.; Borden, E. C.; Fletcher, C. D.; Ryan, C. W.; von Mehren, M.; Blanke, C. D.; Rankin, C.; Benjamin, R. S.; Bramwell, V. H.; Demetri, G. D.; Bertagnolli, M. M.; Fletcher, J. A. Correlation of kinase genotype and clinical outcome in the North American intergroup phase III trial of imatinib mesylate for treatment of advanced gastrointestinal stromal tumor: CALGB 150105 study by cancer and leukemia group B and Southwest oncology group. *J. Clin. Oncol.* **2008**, *26*, 5360−5367.
(18) Wardelmann, E.; Merkelbach-Bruse, S.; Pauls, K.; Thomas, N.; Schildhaus, H. U.; Heinicke, T.; Speidel, N.; Pietsch, T.; Buettner, R.; Pink, D.; Reichardt, P.; Hohenberger, P. Polyclonal evolution of multiple secondary KIT mutations in gastrointestinal stromal tumors under treatment with imatinib mesylate. *Clin. Cancer Res.* **2006**, *12*, 1743−1749.
(19) Heinrich, M. C.; Corless, C. L.; Blanke, C. D.; Demetri, G. D.; Joensuu, H.; Roberts, P. J.; Eisenberg, B. L.; von Mehren, M.; Fletcher, C. D.; Sandau, K.; McDougall, K.; Ou, W. B.; Chen, C. J.; Fletcher, J. A. Molecular correlates of imatinib resistance in gastrointestinal stromal tumors. *J. Clin. Oncol.* **2006**, *24*, 4764−4774.
(20) DiNitto, J. P.; Wu, J. C. Molecular mechanisms of drug resistance in tyrosine kinases cAbl and cKit. *Crit. Rev. Biochem. Mol. Biol.* **2011**, *46*, 295−309.
(21) McLean, S. R.; Gana-Weisz, M.; Hartzoulakis, B.; Frow, R.; Whelan, J.; Selwood, D.; Boshoff, C. Imatinib binding and cKIT inhibition is abrogated by the cKIT kinase domain I missense mutation Val654Ala. *Mol. Cancer Ther.* **2005**, *4*, 2008−2015.
(22) Tamborini, E.; Pricl, S.; Negri, T.; Lagonigro, M. S.; Miselli, F.; Greco, A.; Gronchi, A.; Casali, P. G.; Ferrone, M.; Fermeglia, M.; Carbone, A.; Pierotti, M. A.; Pilotti, S. Functional analyses and molecular modeling of two c-Kit mutations responsible for imatinib secondary resistance in GIST patients. *Oncogene* **2006**, *25*, 6140−6146.
(23) Azam, M.; Seeliger, M. A.; Gray, N. S.; Kuriyan, J.; Daley, G. Q. Activation of tyrosine kinases by mutation of the gatekeeper threonine. *Nat. Struct. Mol. Biol.* **2008**, *15*, 1109−1118.
(24) Gajiwala, K. S.; Wu, J. C.; Christensen, J.; Deshmukh, G. D.; Diehl, W.; DiNitto, J. P.; English, J. M.; Greig, M. J.; He, Y. A.; Jacques, S. L.; Lunney, E. A.; McTigue, M.; Molina, D.; Quenzer, T.; Wells, P. A.; Yu, X.; Zhang, Y.; Zou, A.; Emmett, M. R.; Marshall, A. G.; Zhang, H. M.; Demetri, G. D. KIT kinase mutants show unique mechanisms of drug resistance to imatinib and sunitinib in gastrointestinal stromal tumor patients. *Proc. Natl. Acad. Sci. U. S. A.* **2009**, *106*, 1542−1547.
(25) Jiang, H.; Shao, W.; Wang, Y.; Xu, R.; Zhou, L.; Mu, X. Molecular mechanism of D816X mutation-induced c-Kit activation and -mediated inhibitor resistance in gastrointestinal stromal tumor. *J. Mol. Graphics Modell.* **2018**, *84*, 189−196.
(26) Demetri, G. D.; van Oosterom, A. T.; Garrett, C. R.; Blackstein, M. E.; Shah, M. H.; Verweij, J.; McArthur, G.; Judson, I. R.; Heinrich, M. C.; Morgan, J. A.; Desai, J.; Fletcher, C. D.; George, S.; Bello, C. L.; Huang, X.; Baum, C. M.; Casali, P. G. Efficacy and safety of sunitinib in patients with advanced gastrointestinal stromal tumour after failure of imatinib: a randomised controlled trial. *Lancet* **2006**, *368*, 1329−1338.

DOI: 10.1021/acs.jmedchem.8b01845
J. Med. Chem. XXXX, XXX, XXX−XXX

(27) Demetri, G. D.; Reichardt, P.; Kang, Y. K.; Blay, J. Y.; Rutkowski, P.; Gelderblom, H.; Hohenberger, P.; Leahy, M.; von Mehren, M.; Joensuu, H.; Badalamenti, G.; Blackstein, M.; Le Cesne, A.; Schoffski, P.; Maki, R. G.; Bauer, S.; Nguyen, B. B.; Xu, J.; Nishida, T.; Chung, J.; Kappeler, C.; Kuss, I.; Laurent, D.; Casali, P. G. Efficacy and safety of regorafenib for advanced gastrointestinal stromal tumours after failure of imatinib and sunitinib (GRID): an international, multicentre, randomised, placebo-controlled, phase 3 trial. *Lancet* **2013**, *381*, 295−302.

(28) Serrano, C.; George, S.; Valverde, C.; Olivares, D.; Garcia-Valverde, A.; Suarez, C.; Morales-Barrera, R.; Carles, J. Novel insights into the treatment of imatinib-resistant gastrointestinal stromal tumors. *Target Oncol.* **2017**, *12*, 277−288.

(29) Flynn, D. L.; Petillo, P. A. Modulation of Protein Functionalities. WO2004061084, WO2007008917, US20080248548, 2008.

(30) Swann, S. L.; Merta, P. J.; Kifle, L.; Groebe, D.; Sarris, K.; Hajduk, P. J.; Sun, C. Biochemical and biophysical characterization of unique switch pocket inhibitors of p38alpha. *Bioorg. Med. Chem. Lett.* **2010**, *20*, 5787−5792.

(31) Ahn, Y. M.; Clare, M.; Ensinger, C. L.; Hood, M. M.; Lord, J. W.; Lu, W. P.; Miller, D. F.; Patt, W. C.; Smith, B. D.; Vogeti, L.; Kaufman, M. D.; Petillo, P. A.; Wise, S. C.; Abendroth, J.; Chun, L.; Clark, R.; Feese, M.; Kim, H.; Stewart, L.; Flynn, D. L. Switch control pocket inhibitors of p38-MAP kinase. Durable type II inhibitors that do not require binding into the canonical ATP hinge region. *Bioorg. Med. Chem. Lett.* **2010**, *20*, 5793−5798.

(32) Chan, W. W.; Wise, S. C.; Kaufman, M. D.; Ahn, Y. M.; Ensinger, C. L.; Haack, T.; Hood, M. M.; Jones, J.; Lord, J. W.; Lu, W. P.; Miller, D.; Patt, W. C.; Smith, B. D.; Petillo, P. A.; Rutkoski, T. J.; Telikepalli, H.; Vogeti, L.; Yao, T.; Chun, L.; Clark, R.; Evangelista, P.; Gavrilescu, L. C.; Lazarides, K.; Zaleskas, V. M.; Stewart, L. J.; Van Etten, R. A.; Flynn, D. L. Conformational control inhibition of the BCR-ABL1 tyrosine kinase, including the gatekeeper T315I mutant, by the switch-control inhibitor DCC-2036. *Cancer Cell* **2011**, *19*, 556−568.

(33) Chen, C. T.; Hsu, J. T.; Lin, W. H.; Lu, C. T.; Yen, S. C.; Hsu, T.; Huang, Y. L.; Song, J. S.; Chen, C. H.; Chou, L. H.; Yen, K. J.; Chen, C. P.; Kuo, P. C.; Huang, C. L.; Liu, H. E.; Chao, Y. S.; Yeh, T. K.; Jiaang, W. T. Identification of a potent 5-phenyl-thiazol-2-ylamine-based inhibitor of FLT3 with activity against drug resistance-conferring point mutations. *Eur. J. Med. Chem.* **2015**, *100*, 151−161.

(34) Lee, B. W.; Lee, S. D. [5,5] Sigmatropic shift of N-phenyl-N′-(2-thiazolyl)hydrazines and N,N′-bis(2-thiazolyl)hydrazines into 2-amino-5-(p-aminophenyl)thiazoles and 5,5′-bis(2-aminothiazole) derivatives. *Tetrahedron Lett.* **2000**, *41*, 3883−3886.

(35) Decor, A.; Grand-Maitre, C.; Hucke, O.; O'Meara, J.; Kuhn, C.; Constantineau-Forget, L.; Brochu, C.; Malenfant, E.; Bertrand-Laperle, M.; Bordeleau, J.; Ghiro, E.; Pesant, M.; Fazal, G.; Gorys, V.; Little, M.; Boucher, C.; Bordeleau, S.; Turcotte, P.; Guo, T.; Garneau, M.; Spickler, C.; Gauthier, A. Design, synthesis and biological evaluation of novel aminothiazoles as antiviral compounds acting against human rhinovirus. *Bioorg. Med. Chem. Lett.* **2013**, *23*, 3841−3847.

(36) Cáceres-Castillo, D.; Carballo, R. M.; Tzec-Interián, J. A.; Mena-Rejón, G. J. Solvent-free synthesis of 2-amino-4-arylthiazoles under microwave irradiation. *Tetrahedron Lett.* **2012**, *53*, 3934−3936.

(37) Tan, X.; Tester, R. W.; Luedtke, G. R.; Chakravarty, S.; Mavunkel, B. J.; Perumattam, J. J.; Lu, Q.; Nashashibi, I.; Jung, J.; Hu, J.; Liclican, A.; Almirez, R.; Tabora, J.; Tran, V.; Laney, M.; Levy, D. E.; Dugar, S. Design and synthesis of piperazine-indole p38 alpha MAP kinase inhibitors with improved pharmacokinetic profiles. *Bioorg. Med. Chem. Lett.* **2010**, *20*, 828−831.

(38) Zhao, Z.; Wu, H.; Wang, L.; Liu, Y.; Knapp, S.; Liu, Q.; Gray, N. S. Exploration of type II binding mode: A privileged approach for kinase inhibitor focused drug discovery? *ACS Chem. Biol.* **2014**, *9*, 1230−1241.

(39) Heinrich, M. C.; Maki, R. G.; Corless, C. L.; Antonescu, C. R.; Harlow, A.; Griffith, D.; Town, A.; McKinley, A.; Ou, W. B.; Fletcher, J. A.; Fletcher, C. D.; Huang, X.; Cohen, D. P.; Baum, C. M.; Demetri, G. D. Primary and secondary kinase genotypes correlate with the biological and clinical activity of sunitinib in imatinib-resistant gastrointestinal stromal tumor. *J. Clin. Oncol.* **2008**, *26*, 5352−5359.

(40) Bauer, S.; Yu, L. K.; Demetri, G. D.; Fletcher, J. A. Heat shock protein 90 inhibition in imatinib-resistant gastrointestinal stromal tumor. *Cancer Res.* **2006**, *66*, 9153−9161.

DOI: 10.1021/acs.jmedchem.8b01845
J. Med. Chem. XXXX, XXX, XXX−XXX